Nano Energy 107 (2023) 108122

Contents lists available at ScienceDirect

Nano Energy

journal homepage: www.elsevier.com/locate/nanoen

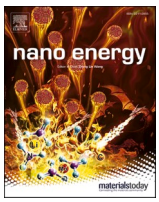

Multiscale in-situ quantification of the role of surface roughness and contact area using a novel Mica-PVS triboelectric nanogenerator

Charchit Kumar [a,*], Jack Perris [a,b], Satyaranjan Bairagi [a], Guanbo Min [a,c], Yang Xu [d], Nikolaj Gadegaard [b], Daniel M. Mulvihill [a,*]

[a] Materials and Manufacturing Research Group, James Watt School of Engineering, University of Glasgow, Glasgow G12 8QQ, UK
[b] Division of Biomedical Engineering, James Watt School of Engineering, University of Glasgow, Glasgow, UK
[c] Bendable Electronics and Sensing Technologies (BEST) Group, James Watt School of Engineering, University of Glasgow, Glasgow G12 8QQ, UK
[d] School of Mechanical Engineering, Hefei University of Technology, Hefei 230009, China

ARTICLE INFO

Keywords:
Triboelectric nanogenerators
Surface roughness
Real contact area
In-situ visualisation

ABSTRACT

Triboelectric nanogenerators (TENGs) are energy harvesters generating electricity via the triboelectric effect and electrostatic induction. However, the influence of interface mechanics on TENG performance requires attention. Here, we study the effect of random multiscale surface roughness on TENG performance using a novel in-situ optical technique to directly visualise the contact interface. To achieve this, a new type of TENG is developed based on transparent mica in contact with polyvinyl siloxane (PVS). A wide range of surface roughness instances were created on the PVS surface (*Sq* from 1.5 to 82.5 μm) by replicating 3D-printed masters developed from numerically generated rough surfaces. TENG output was found to be highly sensitive to surface roughness over a wide range of forces and frequencies. The dependence of real contact area on roughness was identified as the underlying cause. In this work, electrical output (and contact area) decreased significantly with increasing roughness. The highest output (smoothest PVS surface) gave open circuit voltage 222.8 V, short-circuit current density 53 mA/m^2 and peak-power density 4256 mW/m^2: a competitive output given the rapid and simple fabrication, low cost and long durability demonstrated. The new Mica-PVS TENG, the direct technique for TENG interface visualisation and the insights on the role of topography and contact area will be invaluable for future TENG design.

1. Introduction

Sustainable energy generation is a pressing global concern at the present time and critical in our daily lives. As technology becomes increasingly miniaturised and society marches toward a 'smart world' where sensors and various self-powered devices become more popular, the need for sustainable power sources with decreased carbon emissions is clear [1,2]. Currently, batteries are used; however, these are cumbersome and have negative environmental implications [3]. A great way to make use of the world's abundant energy is to utilise devices that can integrate themselves into the surroundings and harness ambient energy. Triboelectric nanogenerators (TENGs) are an emerging and rapidly growing technology that can sustainably harvest electrical power from mechanical energy. TENGs rely on an oscillating contact scenario. During contact, charges transfer across the interface – a phenomenon known as triboelectrification. After separation of the charged planes, an electric field develops and induces charge on backing electrodes via electrostatic induction [4–6]. Connecting with an external circuit causes flow of charge to balance the potential difference. As the gap is closed, current flows in the opposite direction and an AC signal continues as long as the contact cycle repeats. The practical operation of TENGs can be broadly classified into two modes: normal contact-separation mode and sliding mode [6–8]. Over the last decade, TENGs have gained a significant amount of interest from researchers particularly in the materials science and electrical engineering communities. In recent years, a very wide range of material combinations have been trialled in the quest to optimise TENG output [4,9,10]. Usually, selecting materials widely spaced on the triboelectric series (ranking of a material's tendency to gain or lose electrons) promotes a stronger triboelectric effect and yields higher electrical output [11,12]. Polymers are commonly used materials in triboelectric nanogenerators [13]: they offer multiple advantages such as light-weight, flexibility,

* Corresponding authors.
E-mail addresses: Charchit.Kumar@glasgow.ac.uk (C. Kumar), Daniel.Mulvihill@glasgow.ac.uk (D.M. Mulvihill).

https://doi.org/10.1016/j.nanoen.2022.108122
Received 31 October 2022; Received in revised form 3 December 2022; Accepted 18 December 2022
Available online 21 December 2022

energy absorption, and corrosion resistance, just to name a few [14]. Common polymers used in triboelectric systems include polydimethylsiloxane (PDMS), polyethylene terephthalate (PET), polytetrafluoroethylene (PTFE), polyurethane rubber, polyethylene (PE) and polyvinyl chloride (PVC), etc. [13,15–19]. Even though a significant amount of research has been done in the field of TENGs, the interfacial contact mechanics and the role of multi-scale surface texturing on TENG output performance is not well understood yet [4].

In general, the output performance of TENGs is strongly influenced by the physio-chemical characteristics of the contact pair. Parameters such as applied contact pressure, oscillating frequency, surface topography, and real contact area all have a bearing on performance [5,6,9,15,20]. This multi-parameter dependency makes it a complex system to systematically investigate and to independently evaluate the role of individual parameters. For instance, the role of surface roughness has not been systematically explored. However, keeping the same combination of materials and developing multi-scale surface roughness on one of the tribo-surfaces could provide a way to systematically investigate the role of multi-scale topography on the electrical performance of TENGs. Over the last decade, a substantial literature has grown up around device fabrication, and physico-chemical modification of the bulk and surface properties of the tribo-materials. Several researchers have explored functionalisation (such as, silane monolayer deposition and coating) of TENG surfaces to achieve high power output [21–29]. Many others considered various modifications of the bulk tribo-materials: for instance, by developing nano-composites to improve TENG output [22,24,30–33]. Surprisingly, on the mechanics and tribology side, the role and understanding of interface mechanics (at a local microscopic scale) has only recently begun to be addressed [4]. In the triboelectrification process, the contact mechanics of the interacting surfaces is likely to play a crucial role in determining electrical performance. Some interesting recent research has moved in the direction of exploring the effect of different kinds of interface topography. Surface topographies with well-defined and engineered shapes (for example, square, cylinder, half-spherical, pyramid arrays, etc.) have been deployed to explore their effect on TENG performance [34–40]. Choi et al. [34] were able to boost output using nano-pillars on either and both tribolayers (Nickel-PDMS TENG), but the mechanisms remained largely unexplored. Work by Kim et al. [37] used well-defined laser--patterned textures (concave hemispherical shaped) on a PDMS tribo-layer (in contact with aluminium) to optimise TENG performance. Their analysis suggested contact area as the critical parameter in governing the response, but they made no measurements of contact area. In another work by Seol et al. [38], the authors considered pyramid textures on PDMS in (contact with flat Ag). They showed that electrical output increased with contact pressure and later saturated at higher pressures. They also gave a simple optical demonstration of the square contact areas at the pyramid contacts increasing simultaneously as a glass slide was pushed into the surface. All these studies focused on engineered topographies with well-defined structured (non-random) geometries and presented only a qualitative description of the real contact area. However, standard engineering surfaces usually possess multi-scale surface roughness varying from nanometres to a few hundred microns, at different hierarchical levels. In a recent work by Min et al. [15], a systematic study of the role of contact area was carried out for TENGs with random rough surfaces (copper foil and PET). Here, the key finding was that the electrical output (e.g., open circuit voltage and short circuit current) increased with contact pressure in almost the same way as the contact area, with both saturating at approximately the same pressure level – thus, indicating that *real* contact area governs electrical output (mostly because intimate contact promotes electron transfer). Indeed, Xu et al. [20] has successfully modelled the pressure-dependent behaviour of TENGs by combining the mechanics of rough surface deformation with established electrostatic approaches. However, in Min et al. [15], the real contact area measurement was carried out using an indirect method involving insertion of a third body (a combination of two pressure sensitive films) between the tribolayers. In addition, the study by Min et al. [15] looks at only a single surface roughness.

Recent advances in optical visualisation techniques and their growing application in contact mechanics investigations have made it possible to precisely visualise the distribution of real contact junctions down to sub-micron scale and also to investigate the contact dynamics in detail [41–46]. In this paper, we develop a direct in-situ optical contact area visualisation technique for TENGs. This allows for a detailed quantitative description of the contact interfaces during the TENG operation and a simultaneous comparison between electrical power output and real contact area. We then use the technique to systematically investigate the role of multi-scale surface roughness and real contact area (while keeping the tribo-material properties and surface chemistry constant). We begin by developing a new high-performance TENG based on the novel combination of hard (and transparent) mica in contact with soft polyvinyl-siloxane (PVS) – hereafter referred to as a 'Mica-PVS TENG'. PVS is a silicone based viscoelastic polymer. It is a well-known biomaterial and widely used in dentistry to develop tooth imprints [47,48]. Key characteristics of PVS polymer include low-cost, easy commercial availability, simple processing, low modulus, high flexibility, and non-toxicity. Mica, on the other hand, is a hard phyllosilicate mineral characterised physically by a perfect basal cleavage capable of yielding atomically smooth surfaces. It has high dielectric strength and, crucially for the optical visualisation, is transparent.

Surfaces with different scales of surface roughness (ranging Sq from 1 μm to 100 μm) were numerically designed and fabricated on the PVS polymeric material using a combined 3D printing and micro-moulding technique. An electrodynamic mechanical test rig was then modified to perform highly controlled electro-mechanical measurements with a surface self-aligning facility and a reflection interference microscopy-based optical setup to precisely record the distribution of real contact area. The highly accurate setup was also used to quantitatively investigate the effect of contact pressure, oscillating frequency, and external load resistance on TENG output. The work systematically characterises the effect of surface roughness (and contact pressure and frequency) on TENG power output across a wide surface roughness range and interprets the results using direct in-situ contact area measurements. In summary, the key novelties of this work are: the new high-performance TENG based on PVS in contact with mica, the direct optical technique for interface visualisation & contact area measurement in TENGs and the comprehensive study on the effect of multiscale surface roughness on TENG output.

2. Materials, fabrication and testing

2.1. Textured PVS tribo-negative layer fabrication

A number of random rough surface realisations covering a range of areal RMS surface roughness (Sq) values were designed and fabricated. The surfaces were first designed numerically based on a selected power spectrum density using the numerical algorithm reported in Perris et al. [49]. The designed surface topographies closely represent the multi-scale nature of real engineering surfaces. The relevant scales of the surface roughness range from 1 to 100 μm. Four design realisations were created having Sq values of 1.5 (denoted as 'flat'), 25, 50 and 100 μm. A stereolithography (SLA) 3D printing technique (Formlabs Form3 printer, USA) was used to develop textured moulds (surface area = 25 × 25 mm^2) based on the designed surface topographies (Fig. 1a). One could also develop a larger or smaller surface area, if required for a specific application. A controlled thick border of ca. 300 μm in height was created just outside the textured region to achieve a constant thickness for the developed tribo-layers (Fig. 1a). The border edge helps maintain the same active surface area for all tribo-layers. As mentioned, polyvinyl siloxane (or PVS) was used to create the textured surfaces. To the best of the authors' knowledge, PVS has not been used previously in the fabrication of TENGs. PVS is usually used in biomedical (dental)

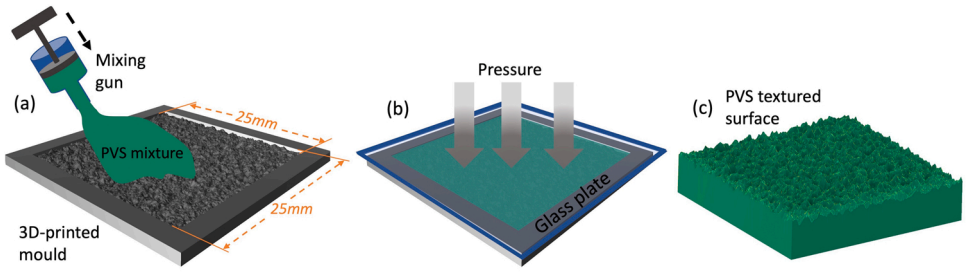

Fig. 1. Schematic of the fabrication procedure to develop PVS tribo-layers with various scales of roughness. Negative moulds with numerically generated multi-scale topographies were manufactured using a stereolithography 3D printer. PVS mixture was slowly poured onto the mould (a) and uniformly pressed with a flat glass plate (b). The textured PVS replica was then slowly peeled off from the mould (c).

applications. Here, we use it because it has good mould replication capability and is a flexible and cost effective tribo-negative material that can be moulded and cured very easily and rapidly. The dielectric constant of PVS was measured at around 3.15. Measurement details and dielectric constant vs. frequency curve (Fig. S1) are provided in the Supporting Information. The PVS (President - The Original, Coltène Switzerland) polymer mixture was slowly poured on the 3D printed moulds using an automatic mixing and dispensing gun and then gently pressed in place using a flat glass plate (maintaining a uniform pressure distribution). While pressing down, the excess polymer mixture comes out of the mould volume. After polymerisation for ca. 10 min at room temperature, the PVS replicas with micro-textures were gently removed from the mould. Produced PVS replicas were then used to form the negative tribo-layer in a contact-separation mode TENG (PVS Tribo-layer in Fig. 2b-c). For convenience, we refer to the four PVS replica samples using the following designation: FlatPVS for the nominally flat PVS surface with $Sq = 1.5$ μm and PVS25, PVS50 and PVS100 for the PVS surfaces having Sq values of 25, 50 and 100 μm, respectively.

2.2. Mica tribo-positive layer and Mica-PVS TENG fabrication

For the tribo-positive layer, we used ultra-smooth ruby muscovite mica thin-sheets (Agar Scientific Ltd, Stansted, Essex, CM248GF, UK) – again, a material little used in TENG research. There are a number of advantages to using mica in the present study. First, thin mica sheet exhibits very high optical transparency, which is crucial for the in-situ optical visualisation of real contact area [42,50,51]– one of the key objectives of our work. Also, mica sheets are easily cleavable and give a highly smooth and atomically flat surface [52]. Combined with the fact that mica is hard (Young's Modulus ≈ 5.4 GPa [53]) in comparison to soft PVS (Young's modules ≈ 3.4 ± 0.2 MPa – see Section 3.4), this allows us to consider the contact as equivalent to a rigid flat in contact with the soft rough surface. Another advantage of mica for TENG construction is its high dielectric strength (κ ≈ 7.0 [54]): higher capacitance of the tribo-layer means greater ability to induce charge on the electrode. The commercial mica sheet comes with a thickness of 150 μm. It was carefully cut into 25 × 25 mm^2 area, using a sharp scalpel. A thin copper tape (3M Copper foil with conductive adhesive, UK) was attached on the back side of the mica tribo-layer, which acts as an electrode. After this, the back side of the copper tape was insulated with an ultra-thin Kapton tape. For the other tribo-layer, the four different textured PVS sheets described in Section 2.1 were used (active area of 25 × 25 mm^2). The PVS sheets were securely pasted on copper tape and then insulated with Kapton tape. A schematic of the TENG device in the test rig is presented in Fig. 2a with photos of the two separate tribo-layers (with connected electrodes) shown in Fig. 2c. Since this study focuses on the role of multi-scale surface roughness and real contact area, it was crucial to keep both samples globally flat. Due to the very low thickness of the tribo-layers (they are easily bended or distorted), all tribo-layers were attached to smooth glass backing plates using transparent double-sided tape. A long copper lead-wire was attached to the electrodes and this was done outside of the active contact region (Fig. 2c) to avoid disturbing the contact formation and pressure distribution. With both tribo-layers having the same active area, the effective dimension of the TENG devices was 25 × 25 mm^2.

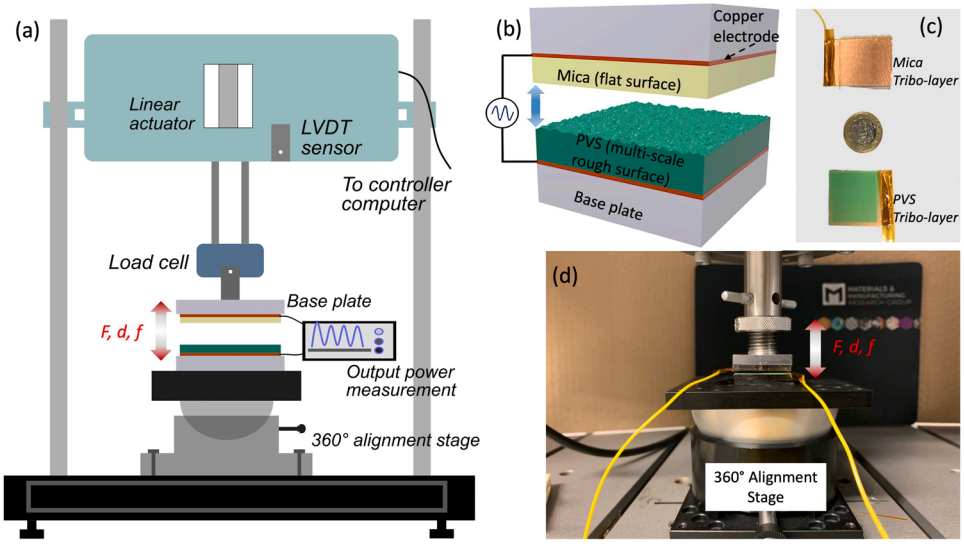

Fig. 2. (a) Schematic of the test rig for high-precision contact-separation TENG measurements, (b) Schematic of the Mica-PVS TENG construction, (c) Photograph of developed TENG tribo-layers and (d) Close-up photo of the test rig around the TENG including the 360° alignment stage. The mica tribo-layer (upper surface) was attached on the base plate and then fixed to an in-house fabricated holder connected to a load cell. The PVS tribo-layer (lower surface) was fixed on the 360° alignment stage. A sample video of the operating test rig is provided in Supplementary Information (Video S1). F = normal force, d = separation distance, and f = oscillating frequency.

2.3. Surface characterisation and mechanical testing of PVS samples

Surface morphology visualisation and characterisation of all PVS samples was carried out using a 3D optical profiler (InfiniteFocus, Alicona-Bruker, Austria). All measurements were carried out at 5x magnification. For the 3D visualisation of captured images, MountainsMap (Digital Surf, France) surface metrology software was used. In addition, 3D printed moulds were quickly visualised under the optical light microscope to check any surface imperfection. A universal compression testing machine (Instron 3367, USA) was used for the mechanical characterisation of PVS material (Supporting Information, Fig. S2). Cylindrical test samples were prepared using the moulding technique. A stress-strain curve was obtained by applying the normal load at a slow loading rate of 1 mm/min. Young's modulus (modulus of elasticity) was then estimated as the slope of stress-strain curve within the proportional limit (straight-line portion). To calculate the Poisson's ratio of PVS, a micro-mechanical testing setup (Dual Leadscrew, Deben, UK) along with a high-definition camera system was used (see Fig. S3 in Supporting Information). An in-situ synchronised video of the polymer sample was recorded during the deformation stage. A digital-image-correlation (DIC) based method (Imetrum Video Gauge, Imtetum, UK) was used to estimate the Poisson's ratio (see Perris et al. [55]).

2.4. TENG testing setup

2.4.1. TENG test rig and electrical measurement

The TENG characterisation work was then carried out in normal contact-separation mode. A detailed schematic of the test rig is presented in Fig. 2a. A high-precision linear electrodynamic fatigue testing machine (Electropuls E3000, Instron UK) was adapted for the tests. A 50 N capacity load cell (tension and compression) was fitted at the actuation drive. A special tribo-surface holder with a flat base was designed and machined to maintain the flatness of the top tribo-layer. Since the work is exploring a flat-on-flat contact configuration, it was crucial to achieve a perfectly parallel contact. To achieve this, a 360° alignment bed was incorporated to attach the lower tribo-layer onto it (Fig. 2d). The alignment bed offers a large degree of freedom in rotation, yawing and pitching along the centre axis. During the development of this test rig, we noticed that a slight alternation in contact alignment could drastically alter the electrical output of the TENGs. The same issue has been reported in a previous work by Hong et al. [56]. Before starting each test, a pre-load (about 10 N) was slowly applied to establish the contact and alignment between the two tribo-layers. Once an aligned contact is established, the lower tribo-layer position was locked by tightening the knob on the adjustable table (Fig. 2d). The test rig is well capable of high frequency oscillations with synchronised data acquisition at high-resolution. Before starting the tests for each type of TENG device, the stiffness of the contacting system was estimated. This is an important step to obtain the correct dynamic impact behaviour via the test machine's feed-back loop. To investigate the effect of contact pressure, normal force was applied ranging from 2 N to 40 N, at a specified cycle frequency. Whereas, for investigating the effect of frequency, oscillating frequency was varied from very low frequency (2 Hz) to a relatively higher frequency of 14 Hz, while keeping contact pressure constant. The test rig allows accurate fixing of the max separation distance (d), which was held at an amplitude of about 2 mm between the peaks of the contact-separation cycles. A digital oscilloscope (RS PRO, Bench-top Mixed Signal Oscilloscope, UK) was used to record the output voltage from the TENG devices. Oscilloscope probes were carefully connected with the TENG electrodes. To measure the current signal from the TENG devices, a low-noise current preamplifier (SR570, Stanford Research Systems, USA) was used and the output signal was acquired with the digital oscilloscope [57]. The open circuit voltage was measured using an electrometer (Keithley, 6517B Digital Multimeter). The surface potential measurements were performed by a non-contact electrostatic voltmeter (Trek Model 347, Trek Inc, USA). The probe was kept steady at a probe-to-surface separation distance of 2 mm. Dielectric property characterisation for the PVS sample (detailed in Supporting Information) was carried out using a LCR metre (Keysight E4980, UK). To systematically assess the output power performance of all four TENGs, we measured the TENG output performance as a function of variable external load resistances (R) over a wide range of 560 Ω – 5 GΩ. All TENG operations were performed at ambient environment conditions.

2.4.2. In-situ optical real contact area measurement

To achieve real contact area visualisation for TENG contacts, a novel setup was developed and incorporated into the TENG testing rig. Owing to one surface being transparent (the mica), the reflection interference microscopy approach could be used to record images of the actual contact interfaces [51,58,59] clearly distinguishing the areas of contact and non-contact. A simplified schematic showing the working principle and optical setup is presented in Fig. 3a. The telecentric lens used provides a unique in-line illumination lighting option. A fibre optic light source was connected to the illumination port to direct the light onto the lens. The optical system is capable of horizontal and vertical resolution of ca. 5.5 μm. It offers a field of view of 11.26 mm × 5.9 mm and this was used as the region for contact area analysis (an area large enough to be representative of the full nominal contact area). The small working distance (40 mm) of the optical lens allowed us to insert the whole optical visualisation system within the compact volume available. A high-definition CMOS sensor camera (Pixelink C-Mount USB 3.0 Camera), with progressive scan and high frame rate, was attached to the telecentric lens and fixed on a focusing stage. Getting a perfect focus is very important to achieve a sharp contrast between the contact and non-contact area. Therefore, after application of normal load, the focus was finely adjusted (Fig. 3a). A representative real contact image captured using this setup is shown Fig. 3b. Regions where two bodies are forming real contacts appear as dark spots, due to destructive interference and bright spots appear at the out-of-contact locations due to the constructive interference.

Recorded real contact images were analysed with *Fiji*, an open-source image processing package based on ImageJ2, (National Institutes of Health, USA). The *Fiji* tool allows for uneven illumination corrections, homogenous filtering, and thresholding procedures [60]. Thresholding was performed based on the pixel grayscale intensity difference between contact and out-of-contact regions (Fig. 3c). All the data analysis and graphing was performed in Python. Owing to the non-transparent nature of the electrodes, the optical images were obtained from separate quasi-static load-up of the TENG samples (without an electrode on the mica) to the contact pressure used for analysis (64 kPa for the TENG tests comparing surface roughness instances in Section 3.3).

3. Results and discussion

3.1. Morphological & mechanical characterisation of tribo-layers

The results of surface morphological characterisation of the PVS tribo-layers are presented in Fig. 4. The surface scans indicate the extent of the range of surface roughness under investigation (i.e. from nominally flat with $Sq = 1.5$ μm to very rough surfaces with $Sq = 100$ μm). The roughness is clearly uniform over the surfaces and there are no problematic imperfections. The root mean square areal surface roughness (Sq) values for the 'as-produced' samples are shown in Table 1 and compared to the design roughness values (see SI for more details on Sq). We note that the as-produced roughness values are somewhat less than the design values: this is likely due to the resolution limitation of the 3D printing technique hampering the realisation of the more steeply sloped features (i.e. those contributing to higher surface roughness) [49]. However, the technique is perfectly adequate for the present purpose which is to achieve rough PVS surfaces covering a wide roughness range. The surfaces comprise an ideal sample-set for our examination of the

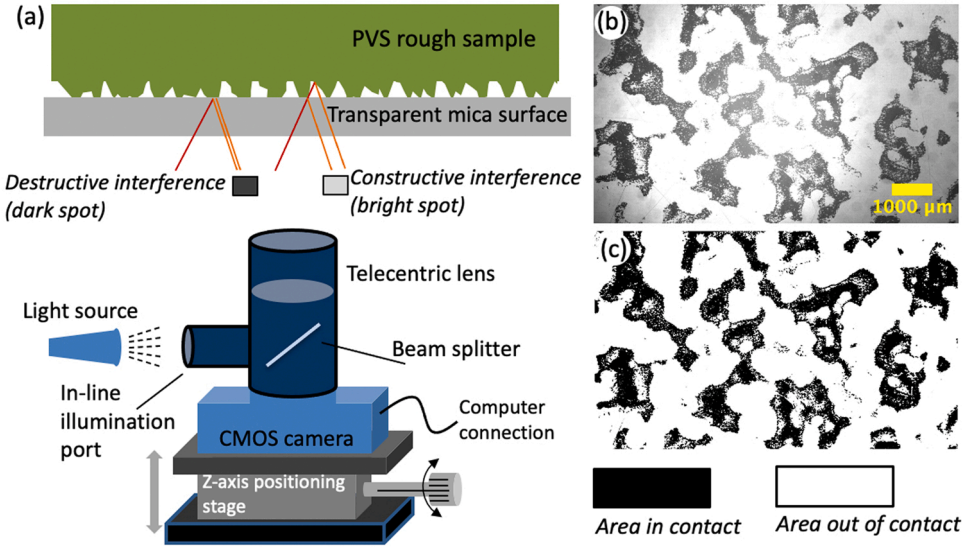

Fig. 3. Schematic of the in-situ optical setup for real contact area measurement between two tribo-layers: (a) A compact telecentric lens with coaxial illumination is attached with high-definition CMOS camera. White light was shone through the illumination port, (b) Sample contact image showing the real contact areas (dark spots) and out-of-contact regions (bright spots) under normal force and (c) Binary image of the real contact image after thresholding.

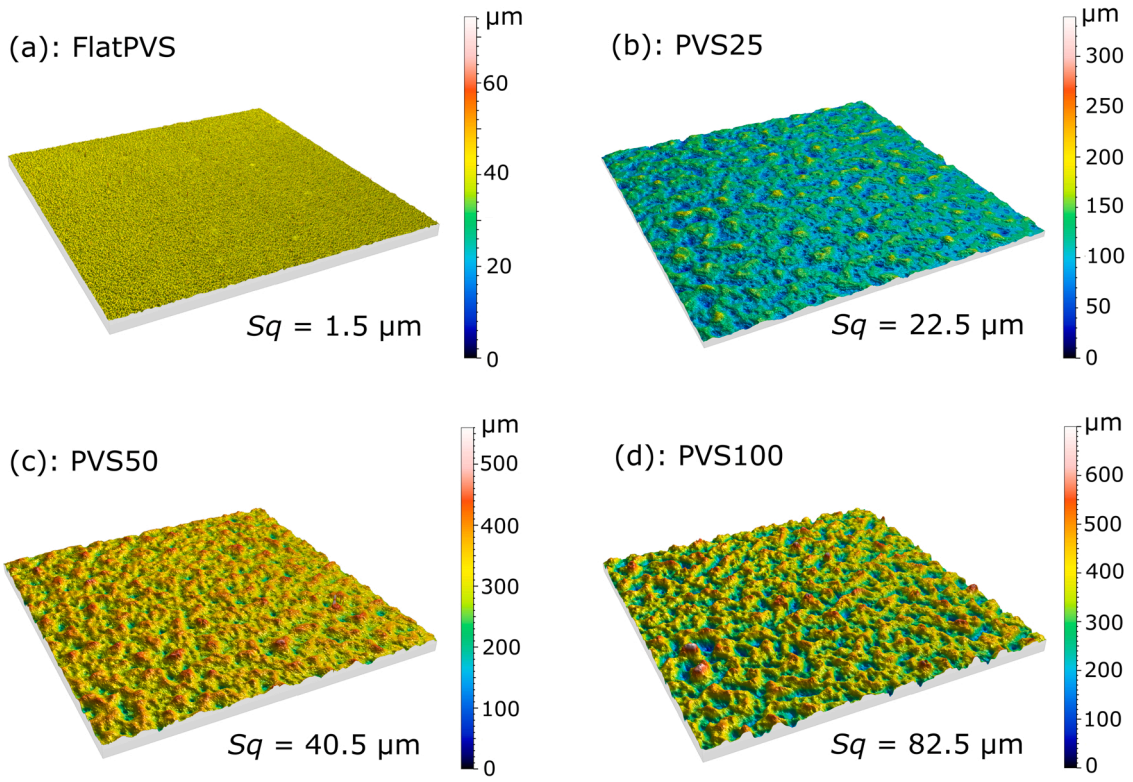

Fig. 4. 3D height maps of the textured PVS tribo-layers: (a) Flat PVS (nominally flat PVS tribo-layer), (b) PVS25 (PVS tribo-layer with design *Sq* of 25 µm), (c) PVS50 (PVS tribo-layer with design *Sq* of 50 µm), and (d) PVS100 (PVS tribo-layer with design *Sq* of 100 µm). Note, the coloured height bar in each image has a different scale range.

role of surface roughness in effecting TENG performance. The method of fabricating the PVS tribo-layers is reliable and robust in producing high-precision controlled textured samples. Indeed, the developed 3D printed mould can be used for rapid production of multiple PVS samples. In addition, the procedure easily allows scaling of the TENG nominal area to produce larger or smaller TENG devices. PVS is a low-cost silicone based soft viscoelastic polymer. The Young's modulus and Poisson's ratio of the PVS material was experimentally measured at 3.4 ± 0.2 MPa and 0.45 respectively. The complete stress-strain curve obtained from the mechanical testing of PVS is provided in the Supporting Information (Fig. S4). A key advantage of using PVS lies in its ultra-fasting curing time (ca 0.10 min), simple handling and easy processing [61]. PVS tribo-samples could be developed without using any expensive and sophisticated machinery. Before discussing the results of the in-situ optical characterisation of the TENG interface, we first

Table 1
Root mean square areal surface roughness (*Sq*) of the 'as produced' PVS tribo-layers compared with the numerically generated design values.

Surface type	Numerically generated design roughness *Sq* (μm)	PVS Tribo-layer surface roughness *Sq* (μm)	Abbr.
PVS tribo-layer with nominally flat surface	–	1.5	FlatPVS
PVS tribo-layer with 25 μm micro-textures	25	22.5	PVS25
PVS tribo-layer with 50 μm micro-textures	50	40.5	PVS50
PVS tribo-layer with 100 μm micro-textures	100	82.5	PVS100

explore the contact pressure and frequency dependence of the Mica-PVS TENG and how these are effected by roughness.

3.2. Effect of contact pressure and frequency

To systematically investigate the effect of the nominal contact pressure, TENG measurements were carried out at nine different contact forces (F varying from 2 N to 40 N), by maintaining all other process parameters (such as oscillating frequency, separation distance and contact cycles) constant. This corresponds to nominal contact pressure (p_n) values of 3.2, 8, 16, 24, 32, 40, 48, 56 and 64 kPa. Nominal contact pressure is calculated as F/A_n where A_n is the nominal contact area (25 × 25 mm^2). In general, TENG research is usually carried out at different normal forces and nominal areas [15]; therefore, calculating the nominal contact pressure allows for a more meaningful comparison. The working mechanism of the PVS-Mica TENG is schematically demonstrated in Fig. S5 in the Supporting Information. Fig. 5 shows peak-to-peak output voltage (V_{out}) vs time for the Mica-FlatPVS TENG at different nominal contact pressures. The output voltage was recorded after a few hundred cycles (at the stable functioning stage). After running the TENG device at a given condition, the tribo-layers were kept relaxed for few minutes to allow time for the material to relax. This is especially important when one of the tribo-layers (PVS) is a viscoelastic material [42]. A notable feature of Fig. 5 is the symmetric (about the zero voltage level) and uniform voltage peak output signal (at all pressures). Given the authors experience with other testing setups (e.g. using mechanical shakers etc.), this result appears to have been due to careful setup and use the self-alignment feature combined with the accurate and

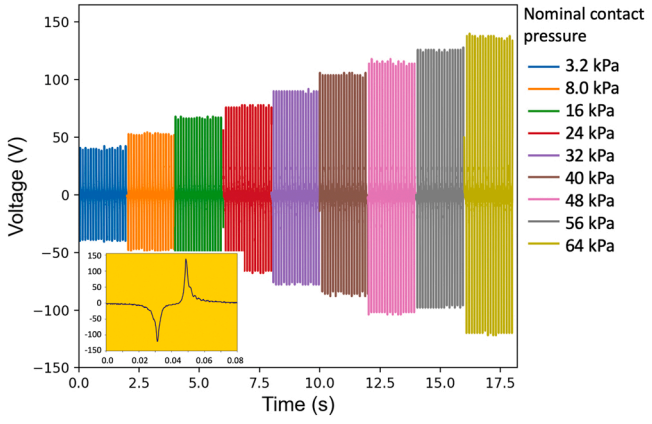

Fig. 5. Output voltage versus time signals over a range of applied nominal contact pressures for the Mica-FlatPVS TENG. Inset represents the zoomed-in view of the voltage signal for a single contact-separation cycle.

precisely controlled motion of the electrodynamic test machine. The authors contend that the non-symmetric and non-uniform voltage output commonly observed in reported TENG results is often due to poor alignment and fluctuating contact conditions. There are different opinions here: a recent work by Dharmasena et al. [62] investigated the asymmetry in TENG current output and attributed it to the adhesion induced impulsive separation of tribo-layers.

Looking closely at the contact and separation cycle (see Fig. 5 inset for a single cycle), the dynamics of contact formation and separation seem very smooth, without any major disturbance in the electrical output signal. To study the effect of nominal contact pressure over a wide range of oscillating frequency, each set of contact loading conditions was performed at four different frequencies: 3, 5, 7 and 9 Hz. For all four TENGs (Mica-FlatPVS, Mica-PVS25, Mica-PVS50 and Mica-PVS100), V_{out} values are plotted against nominal contact pressure for four different frequencies in Fig. 6. It is clear from the results that V_{out} increases with increasing contact pressure, regardless of tribo-layer surface roughness or oscillating frequency. This contact pressure-dependent behaviour of V_{out} has been noted previously [15,38,63,64]. It is understood to be due to the *real* contact area increasing with pressure – a phenomenon well accepted in the tribology literature [41,42,65,66]. Indeed the results in Min et al. [15] clearly indicate that electrical output tracks real contact area as contact pressure is increased. It is considered that the total surface tribo-charge increases when the real contact area increases – thus leading to the increase in output voltage. Interestingly, if we closely examine the pressure dependent results in Fig. 6, the sensitivity of output voltage to contact pressure (slope of the graph) appears to be frequency dependent with the lowest frequency (3 Hz) being least sensitive to pressure.

To better visualise and compare between TENGs having different PVS roughness, V_{out} is plotted at a constant oscillating frequency of 7 Hz in Fig. 7 for each roughness case. It is clear from the results that the Mica-FlatPVS TENG exhibits the highest output voltage for the whole contact pressure range (3.2 – 64 kPa) investigated. For FlatPVS, V_{out} was 43.2 V at 3.2 kPa and increased by about seven times to 316 V when the contact pressure was increased to 64 kPa. By fitting a linear trend-line on the Mica-FlatPVS data-points, a sensitivity of about 8 V/kPa results (highest out of all four TENGs). However, the sensitivity of output voltage to contact pressure decreases as the surface roughness increases on the PVS tribo-layers with the PVS100 (highest surface roughness case) exhibiting the lowest sensitivity of about 1.6 V/kPa. This is likely to be due to the amount of *real* contact area being more sensitive to pressure for smoother surfaces (where the initial contact area at low pressures is sparse, but can increase quickly as load is applied). This phenomenon could be further explained using the Greenwood-Williamson rough contact model or Persson's theory [67]. According to this model, at low pressure loading situations, the real contact area evolution can be estimated by following equation:

$$A_r = \frac{\kappa}{\sqrt{\langle |\nabla h|^2 \rangle}} \frac{\bar{p}}{E^*} \tag{1}$$

where $\langle |\nabla h|^2 \rangle$ is the surface gradient, κ is a constant of $\sqrt{2\pi}$ and $\sqrt{\frac{8}{\pi}}$ and E^* is plane strain modulus. Assuming the (mean) charge density is constant, then the slope of output voltage vs. average contact pressure is proportional to the partial derivative of real contact area with respect to average contact pressure, i.e., $\frac{\kappa}{\langle |\nabla h|^2 \rangle E^*}$. Since work by Perris et al. [49] showed that the surface gradient increases with increasing the *Sq*, it is expected that the slope of output voltage decreases with *Sq*. The surface roughness-dependent pressure sensitivity of the output voltage in Fig. 7 will be an important consideration for those designing TENG based pressure sensors – as sensitivity can clearly be adjusted by surface roughness.

The frequency of contact-separation is a crucial parameter influencing TENG performance. For efficient and versatile operation, TENGs

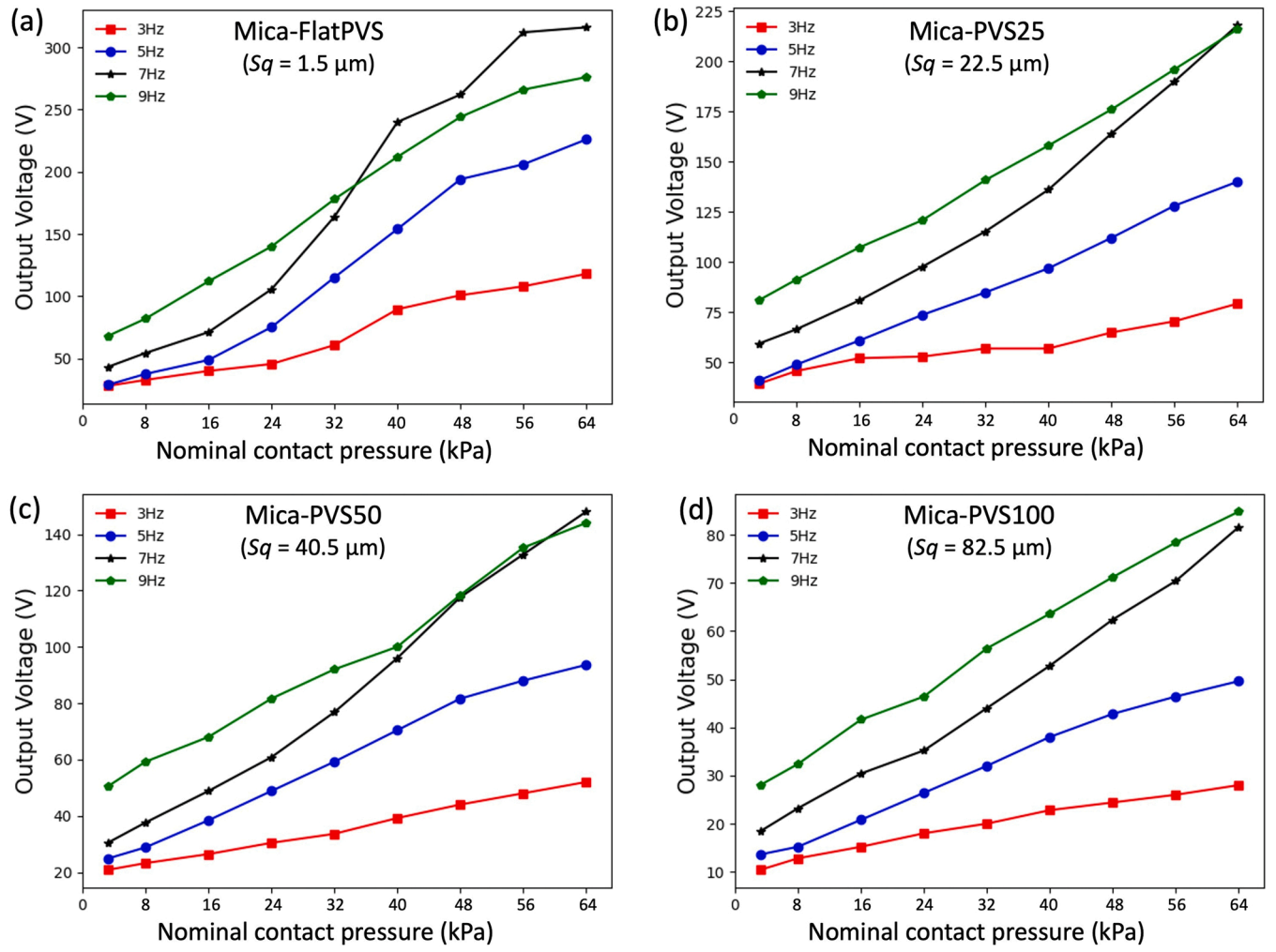

Fig. 6. Effect of the nominal contact pressure on peak-to-peak output voltage (V_{out}) at four different oscillating frequencies: 3 Hz, 5 Hz, 7 Hz, and 9 Hz: (a) Mica-FlatPVS, (b) Mica-PVS25, (c) Mica-PVS50, and (d) Mica-PVS100. Note the different *y*-axis scaling on each graph.

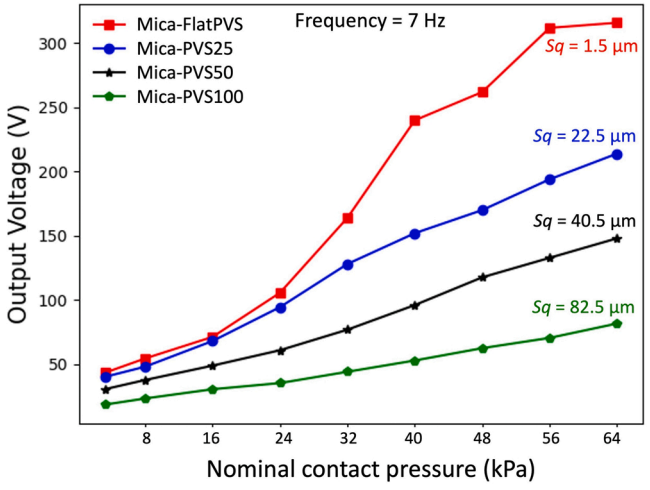

Fig. 7. Sensitivity of output voltage (peak-to-peak) to contact pressure for different surface roughness magnitudes (ranging from design *Sq* of 1.5 µm (Mica-FlatPVS) to 100 µm (Mica-PVS100). All tests were performed at a constant oscillating frequency of 7 Hz and separation distance of 2 mm.

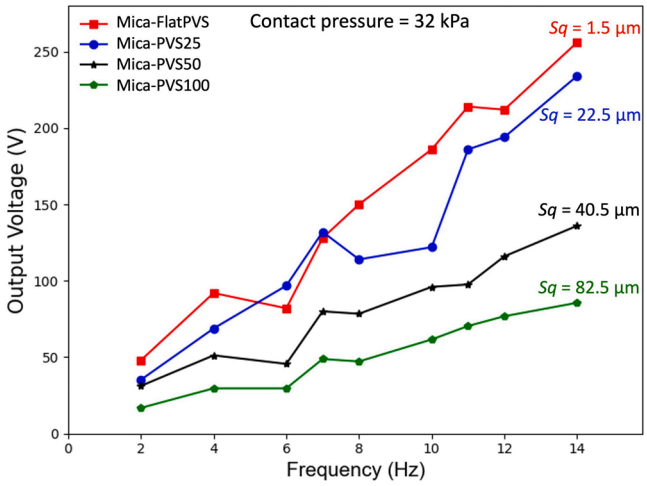

Fig. 8. Sensitivity of output voltage (peak-to-peak) to oscillating frequency for different surface roughness magnitudes (ranging from design *Sq* of 1.5 µm (Mica-FlatPVS) to 100 µm (Mica-PVS100). All measurements were carried out at a constant nominal contact pressure of 32 kPa and separation distance of 2 mm.

should be able to produce power in multi-frequency situations. To evaluate the frequency dependence of output voltage and the effect of surface roughness, the voltage vs. frequency is plotted for each surface roughness case in Fig. 8 at a contact pressure of 32 kPa and separation distance of 2 mm. As shown, peak-to-peak output voltage (roughly) linearly increases with increasing frequency. The increase of TENG output with frequency has been noted before and can be attributed to two sources: the accumulation and retention of tribo-charges which are not neutralised during the shorter contact time associated with high frequency contacts and the obvious increase in current due to moving charges in a shorter timescale (as $I = dQ/dt$) [68,69]. The Mica-FlatPVS TENG (lowest PVS roughness) exhibited the highest output voltage and the Mica-PVS100 TENG (highest PVS roughness) produced the lowest output voltage over the whole frequency range investigated. As we shall see later (Section 3.3), this is because the rougher surfaces generate less real contact area (i.e. less sites for charge transfer). For instance, at the lowest oscillation frequency ($f = 2$ Hz), the V_{out} for the Mica-FlatPVS TENG was 48 V, but was only 16.8 V for Mica-PVS100 (and for $f =$ 14 Hz, the equivalent output voltages were 256 V for Mica-FlatPVS and only 85.6 V for Mica-PVS100). Again, a simple linear fit was used to determine the frequency sensitivity of the output voltage in each roughness case. As with contact pressure, the sensitivity of the output voltage to frequency appears to be surface roughness dependent. The Mica-FlatPVS has the highest sensitivity (about 17.6 V/Hz) while the Mica-PVS100 has the lowest (about 5.9 V/Hz). Finally, these frequency dependent output results (Fig. 8) suggest an approach to fine control TENG electrical output by adjusting the applied oscillating frequency for application-specific power requirements.

3.3. Role of surface roughness and real contact area

The short circuit current (I_{sc}) and open circuit voltage (V_{oc}) are the maximum current and maximum voltage produced from a TENG device [69]. In real engineering applications, an electrical load is connected to the power generating device (TENG) and it's power output can change depending on the external load resistance [69–72]. TENG output (voltage and current) characteristics were recorded at a large range of external load resistances (R) ranging from 560 Ω to 5 GΩ. To facilitate a systematic comparison of electrical output between the TENGs with the four different PVS roughness values (Mica-FlatPVS, Mica-PVS25, Mica-PVS50, and Mica-PVS100), the contact-separation tests were run at exactly the same operating conditions: $p_n = 64$ kPa, $f = 7$ Hz, and $d = 2$ mm. Electrical power output against external load matching results are presented in Fig. 9 for each (PVS) surface roughness. As expected (Fig. 9a-d), the voltage progressively increases with external load resistance for all four roughness cases. The voltage saturates at high resistance values of about 100 MΩ - 5 GΩ. Note that, when the load resistance is very large, the circuit can be considered as an open circuit. The corresponding voltage value can then be regarded as the open circuit voltage, V_{oc} [71]. The V_{oc} value for the Mica-FlatPVS TENG was recorded at 222.8 V at the resistive load of 5 GΩ: this represents the highest open-circuit voltage recorded. Open circuit voltage values of 216.5 V, 167.6 V and 119.7 were recorded for PVS25, PVS50 and PVS100, respectively (Fig. 9). Clearly, the V_{oc} reduces with increasing roughness on the PVS tribo-layer – we will probe this further later.

Results on current-load ($I - R$) investigation (red plots in Fig. 9a–d) show the peak-to-peak current decreasing with increasing external

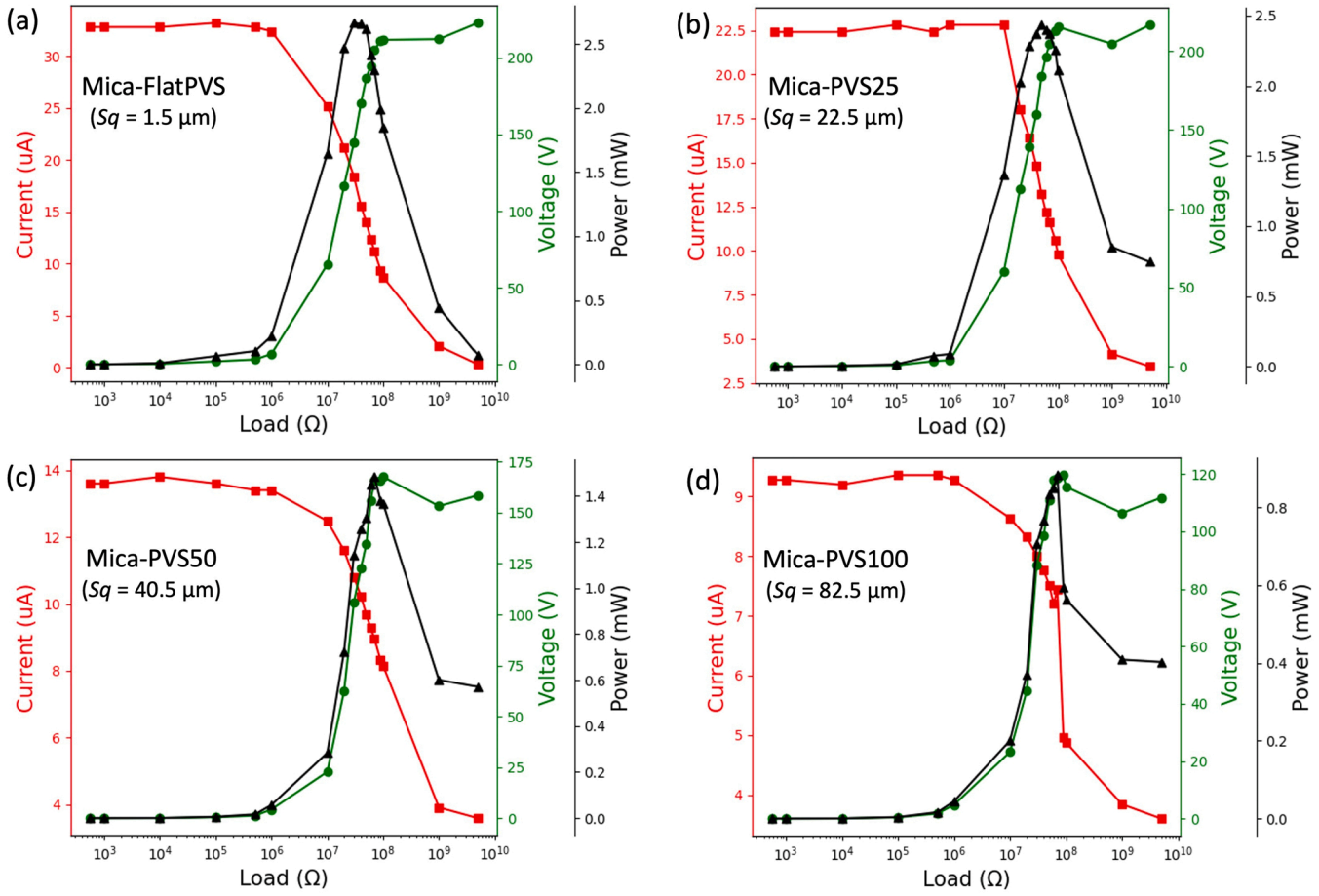

Fig. 9. Effect of external load resistance on current, voltage and power output from the TENGs with different roughness on the PVS layer: (a) Mica-FlatPVS ($Sq =$ 1.5 µm), (b) Mica-PVS25 ($Sq = 22.5$ µm), (c) Mica-PVS50 ($Sq = 40.5$ µm), and (d) Mica-PVS100 ($Sq = 82.5$ µm). Note that the y-axes in all four graphs have different ranges.

resistance and reaching the lowest value (nearly zero) at the highest R (~5 GΩ). This is simply attributed to very high ohmic losses at high resistance [7,71]. The current value recorded at the very low (or negligible) R can be considered as the I_{sc} [69]. The maximum I_{sc} of 33.2 μA was measured for the Mica-FlatPVS TENG at a low value of R (~100 kΩ). I_{sc} then decreased with increasing surface roughness to 22.8 μA, 13.8 μA and 9.36 μA for PVS25, PVS50 and PVS100, respectively. Instantaneous power was calculated using the recorded voltage and current ($P = V \times I$) at each external load resistance. Power output against load resistance exhibits the characteristic n-shaped curve reported in previous work [7,30,70,73,74]. For all the four TENG devices, the P_{max} was achieved in the range 30 MΩ – 70 MΩ external load resistance.

To probe the effect of surface roughness on TENG output, the power versus resistance curves are compared in Fig. 10a. The overall maximum peak power (P_{max}) was recorded at 2.66 mW for the Mica-FlatPVS TENG device at 30 MΩ (dark blue plot in Fig. 10a). Peak power then reduced significantly with surface roughness to 2.4, 1.5 and 0.9 mW for PVS25, PVS50 and PVS100, respectively. This represents an almost 70% reduction in peak power output going from the Mica-FlatPVS to the Mica-PVS100 TENG. Note that the maximum peak power output (2.66 mW) for the Mica-PVS TENG corresponds to a maximum peak power density of 4256 mW/m^2. To shed light on this dramatic surface roughness dependent response, we captured high-definition in-situ optical images of the interfacial *real* contact area at the fixed 64 kPa contact pressure for each roughness case. Fig. 10b-e shows the binarized real contact images for all four roughness instances (Mica-FlatPVS, Mica-PVS25, Mica-PVS50 and Mica-PVS100) and each interface image corresponds to a power versus resistance plot in Fig. 10a. The corresponding raw images are provided in Supporting Information (Fig. S6). It is worth pointing out here that the real contact visualisation technique nicely shows the distribution of real contact area and is perfectly able to distinguish between regions of *real* contact (dark spots in Fig. 10b-e) and the out-of-contact regions (bright areas in Fig. 10b-e). Achieving direct and accurate real contact visualisation on multi-scale rough contact interfaces is challenging. Min et al. [15] investigated the contact area in a TENG having nominally flat Cu and PET tribo-layers. However, the approach was indirect using a third body (pressure sensitive film) between the contact. Lee et al. [75] utilised an ink-transfer based approach, however the resolution remained unclear. A few other

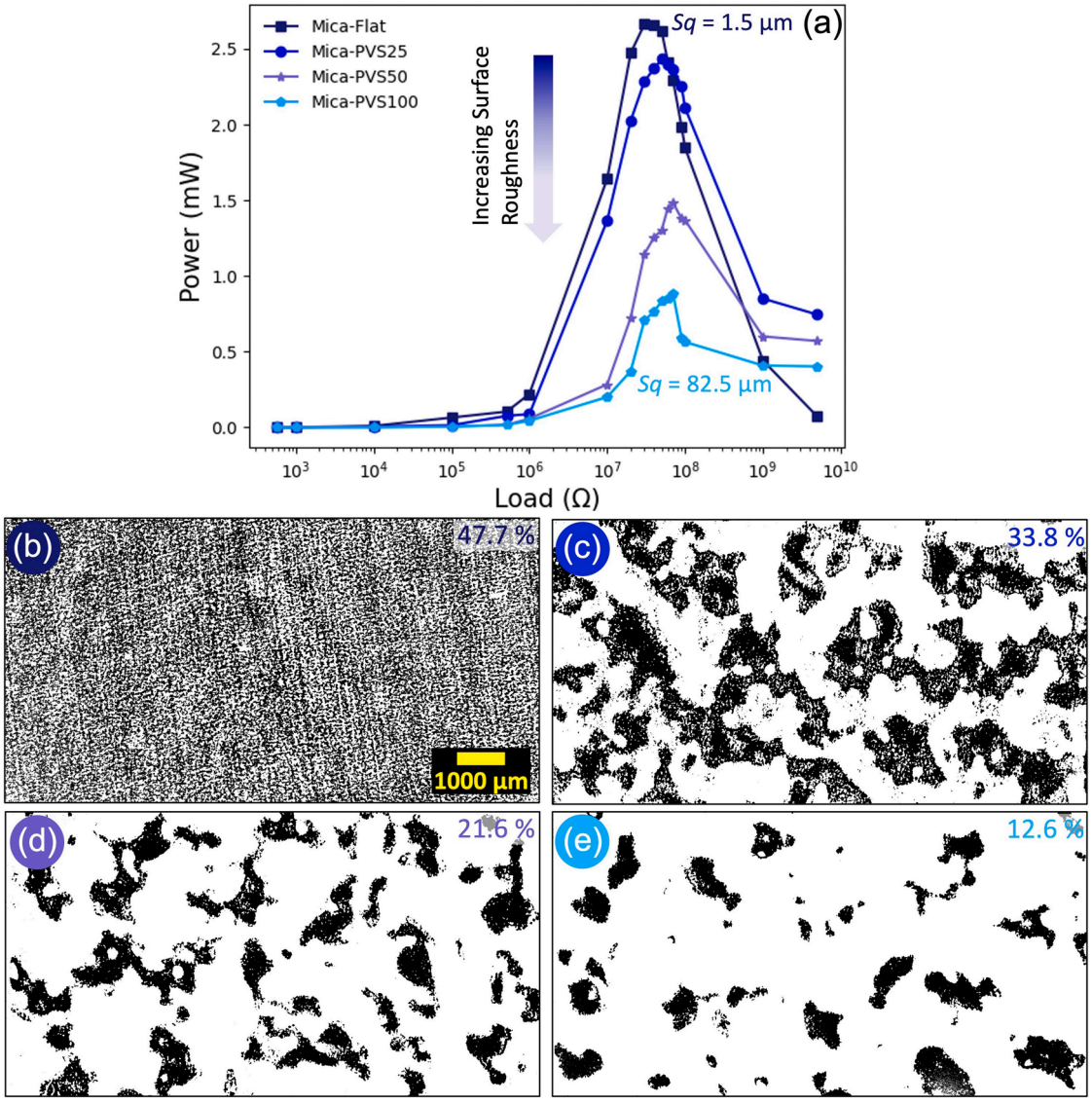

Fig. 10. (a) Comparison of power output versus external load resistances from all four different TENG devices. High-definition contact images (binarized) during the contact formation of TENG on all four tribo-layers at a nominal contact pressure of 64 kPa. (b) Flat PVS, (c) PVS25, (d) PVS50 and (e) PVS100. Black spots showing the real contact area and bright areas represent the out-of-contact zones. Scale bars are the same for each image as given in the image 'b'.

researchers qualitatively observed the contact area in TENGs, but on regular and defined structured surfaces [36,39]. It is clear from the visuals in Fig. 10 that contact area reduces dramatically as the roughness is increased from the smooth Mica-FlatPVS case (Fig. 10b) to the rough Mica-PVS100 case (Fig. 10e). However, to quantify the amount of contact, we define the real contact area percentage as:

$$\text{Real contact } area\ \% = \frac{Real\ contact\ area\ (A_r)}{Nominal\ contact\ area\ (A_n)} \times 100 \quad (2)$$

The real contact area (A_r) is the sum of all the areas forming real solid-solid contact (black spots in Fig. 10b-e) and the nominal contact area (A_n) is simply the apparent area of the imaged area for analysis. Real contact area and peak power are plotted together against PVS tribolayer surface roughness in Fig. 11. The Mica-FlatPVS TENG exhibited the highest real contact area percentage (47.7%). Real contact area percentage then reduced with increasing surface roughness to 33.8%, 21.6% and 12.6% for PVS25, PVS50 and PVS100, respectively. The reason for this is clear from the images in Fig. 10. For the Mica-FlatPVS TENG, the roughness is very low ($Sq = 1.5$ μm) and this permits a large contact area (Fig. 10b), but for the Mica-PVS100 TENG, roughness is high ($Sq = 82.5$ μm) and far less contact is formed due to the steep slopes and deep valleys on the surface. The crucial result is that peak power output closely tracks real contact area in the plots against surface roughness in Fig. 11. Thus, the underlying explanation for the roughness-dependent power output is the following. As roughness increases, contact area decreases and this reduces the amount of transferred charges across the interface thereby reducing power. Furthermore, we measured the surface potential of all four PVS tribolayers (Mica-FlatPVS, Mica-PVS25, Mica-PVS50, and Mica-PVS100), after forming a contact at a nominal contact pressure of 64 kPa. Surface potential results are presented in Fig. 11b. For all four tribo-layers, the surface potential gradually decays over the time. This surface potential decay behaviour may be due to the lateral spreading of surface charges, bulk transportation (conduction) into the material and charge neutralisation with ions in the environment. [76–78]. The initial surface potential exhibits a decreasing trend with increasing surface roughness on the PVS tribolayers. Initial surface potential values were measured at about 2320 V, 2160 V, 1480 V and 1080 V for Mica-FlatPVS, PVS25, PVS50 and PVS100 tribolayers, respectively. The reason for reduction in the surface potential with high surface roughness on the PVS tribo-layers is likely attributable to the reduced real contact area contributing towards tribo-electrification (which should result in lower surface charge). Interestingly, the surface potential reduction trend follows the same trend observed for power output and real contact area (in Fig. 11a). These surface potential results support our argument on the critical role of surface roughness and real contact area in governing the electrical performance of TENGs. Analysis of the contact visuals during the dynamic contact-separation cycle, indicated that the attachment and detachment phases were very smooth and stable. No explicit disturbances or sudden fluctuations were noticed and we did not observe any bending deformation. We believe that the smooth attachment and detachment contributed to the symmetric, uniform and noise-free electrical output signals shown in Fig. 5. In addition, the distribution of contact areas in Fig. 10b-e is very uniform indicating excellent alignment (even for the smooth flat case in Fig. 10b).

Although electrical output decreased with increasing surface roughness in the present study, this is not a universal conclusion and the response to surface roughness can be rather subtle. In fact, when surface roughness is increased, the real contact area between two contacting bodies may decrease or increase as compared to the idealised nominal smooth flat-on-flat contact depicted in Fig. 12a. This depends on a number of factors such as the relative mechanical properties of the contact bodies, surface energy, interfacial loading conditions and on which surface the roughness was introduced (i.e. on the softer or harder surface) [65,79,80]. In this work, surface roughness was introduced on the softer tribo-layer (the PVS) and the counter contact surface (mica) was atomically flat. PVS is significantly softer than mica (Young's modulus of PVS and mica and are 3.4 ± 0.2 MPa and 5.4 GPa, respectively) [53]. This is somewhat equivalent to flattening a roughened soft surface by a rigid flat: at low and moderate loads, contact area will only occur around the higher roughness features. Therefore, the case in the present work corresponds to Fig. 12b. On the other hand, if we press a hard (rigid) rough surface into a soft flat surface to form a conformal contact, a contact area greater than even the nominal contact area is achievable (as indicated in Fig. 12c). This type of contact configuration has been reported in the literature [81–84]. Such real contact area enhancement could be used to advantage in future TENG design if the right combination of materials and topography are selected for the tribo-layers. A hard rough surface pressed into a soft surface will likely produce a 3D contact area – it is not possible to visualise this using the optical technique in the present paper but an investigation of this contact scenario in TENGs would make an interesting future study. These results on power output and real contact area suggest the real contact area is a crucial parameter to consider in the optimisation TENG performance.

Interestingly, Qiao et al. [85] showed that, if a high flexoelectric effect is present (i.e. high electrical polarisation in response to strain gradients in the material), then rougher surfaces (pyramid arrays in this

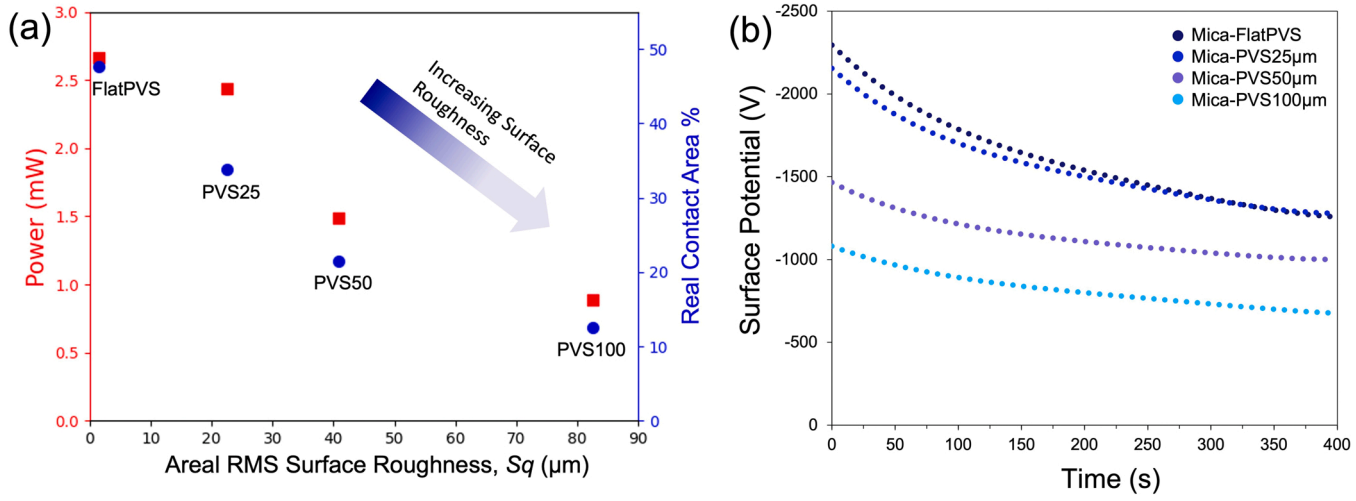

Fig. 11. (a) Peak power output (P_{max}) and real contact area % versus the areal RMS surface roughness (Sq) of the PVS tribo-layers. Nominal contact pressure was fixed at 64 kPa and (b) Surface potential vs time curves for all four PVS tribolayer roughness instances.

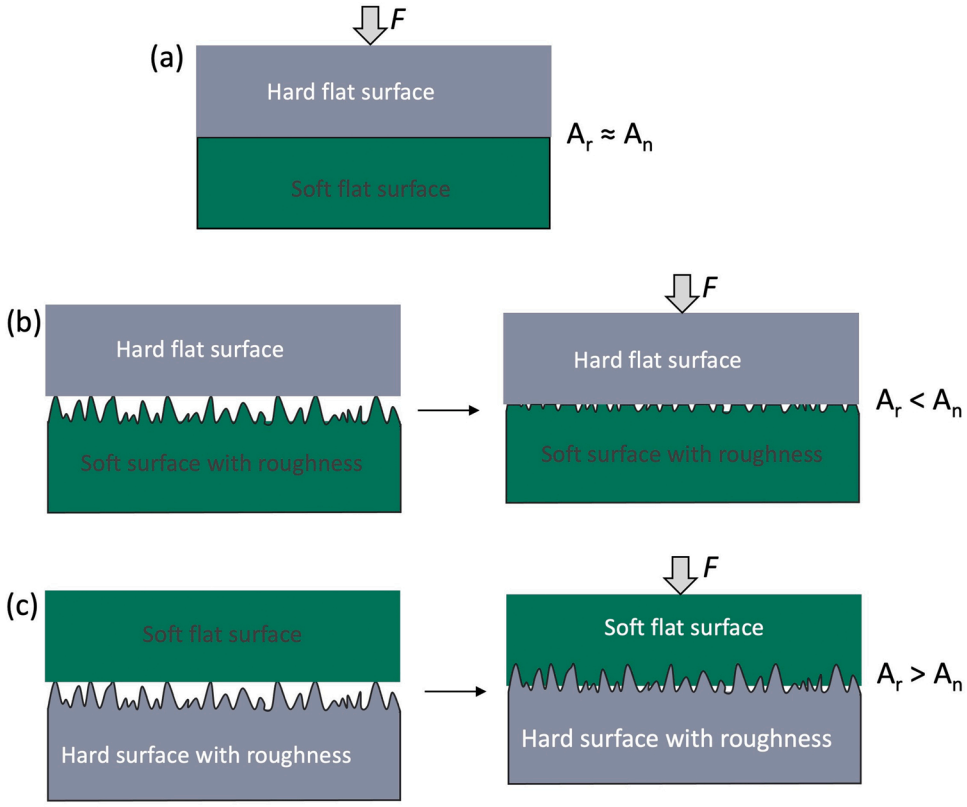

Fig. 12. Schematic diagram indicating how difference in TENG tribo-layer hardness might affect the difference in TENG response to increasing surface roughness: (a) real contact area A_r approaching the nominal contact area A_n (i.e. $A_r \approx A_n$) is theoretically possible if the surfaces could approach the ideally flat case of zero roughness (not possible in reality), (b) contact area is lowered (compared to (a) – i.e. $A_r < A_n$) when a hard smooth surface is pushed into a soft rough surface and (c) contact area can actually be increased (compared to (a) – i.e. $A_r > A_n$) when a soft flat surface is pushed into a rough hard surface.

case) can produce higher or lower TENG output (compared to flat-flat) depending on whether the flexoelectric and triboelectric effects add or subtract from each other. However, the appearance of a notable flexoelectric contribution may be limited to materials exhibiting a high flexoelectric coefficients.

3.4. PVS-Mica: a regenerative TENG, device stability and application

To examine the stability and durability of the Mica-PVS TENG, continuous contact-separation operation was performed at a nominal contact pressure of 56 kPa and oscillating frequency of 7 Hz. The output voltage was continuously recorded from the beginning of the durability test. Long-run stability and durability test results are presented in Fig. 13a and results clearly show that the Mica-PVS TENG device can run efficiently for more than 26,000 cycles without showing any decay in electrical output. The output performance ($V_{out} \approx 240$ V) of the Mica-PVS TENG remained highly stable and uniform throughout the operation (Fig. 13a(i) & a(ii)). The long durability of the Mica-PVS TENG lies in the combination of hard and soft tribo-layer materials, which tend to exhibit highly stable mechanical response under continuous cyclic loading [86,87] (the PVS is highly soft and compliant with Young's modulus of 3.4 ± 0.2 MPa; whereas, the mica is much stiffer and harder with Young's modulus of 5.4 GPa [53]).

Usually, mica sheet is easily cleavable using a scalpel and offers a highly flat (atomically smooth) and clean surface area [50]. After running several thousands of contact-separation cycles on the Mica-FlatPVS TENG, an ultra-thin layer was carefully cleaved from the bulk mica. Interestingly, after cleaving off a layer of mica (at about 26,000 cycles), the Mica-PVS TENG showed a surprising jump in output (V_{out} from 240 to 278 V) as compared to the earlier un-cleaved situation (See Fig. 13a). A possible explanation for the increment in power output after cleaving may be the fact that, the freshly cleaved mica is extremely clean and contamination free and facilitates a more intimate contact against the contacting PVS surface (the mica prior to cleaving will have been exposed to the ambient atmosphere for a long time and may have accumulated adsorbed molecules and dust particles). Moreover, pristine mica (i.e. obtainable after cleaving) exhibits a very high surface energy and wettability which could also serve to increase real contact area via increased adhesion [52,88]. This unusual property even leads to the interesting prospect of a regenerative TENG. We also performed the stability test on the regenerative Mica-PVS TENG, and corresponding results confirmed high stability and continuous power generation for more than about 12,000 additional contact-separation cycles (Fig. 13a (iii) & a(iv)). Indeed, the Mica-PVS combination with the regenerative aspect could facilitate long stable power output options.

In order to investigate the self-powering ability of the Mica-PVS TENG, a wide range of commercial capacitors (capacitance: 1 μF, 2.2 μF, 10 μF, 22 μF, 47 μF and 100 μF) were charged at a nominal contact pressure of 64 kPa and an oscillating frequency of 7 Hz. Fig. 13c shows the capacitor charging characteristics and confirms the smooth output behaviour during charging. Charging (oscillation on) and discharging (oscillation off) cycles with the 1 μF capacitor is presented in Fig. 13d. Next, we offer a brief demonstration of the Mica-FlatPVS TENG operating various low-power electrical devices. A pattern of 42 large-sized (5 mm diameter) commercial LEDs (as the external load resistance) connected in series were simultaneously illuminated (Fig. 13e). A full video of the LED illumination is provided in the Supporting Information (Video S2). To convert the AC signals generated from the TENG to usable DC output, a bridge rectifier was attached between the TENG device output and the LED circuit, as shown in Fig. 13e. Furthermore, a commercial calculator (Fig. 13f), a digital alarm clock (Fig. 13g) and a digital vernier caliper (Fig. 13h) were successfully powered using the Mica-FlatPVS TENG through a 100 μF capacitor (corresponding circuit diagram is presented in Fig. S7). Full videos of each application are provided in the Supporting Information (Video S3-S5).

Supplementary material related to this article can be found online at doi:10.1016/j.nanoen.2022.108122.

Overall, the Mica-PVS TENG, demonstrates a competitive output

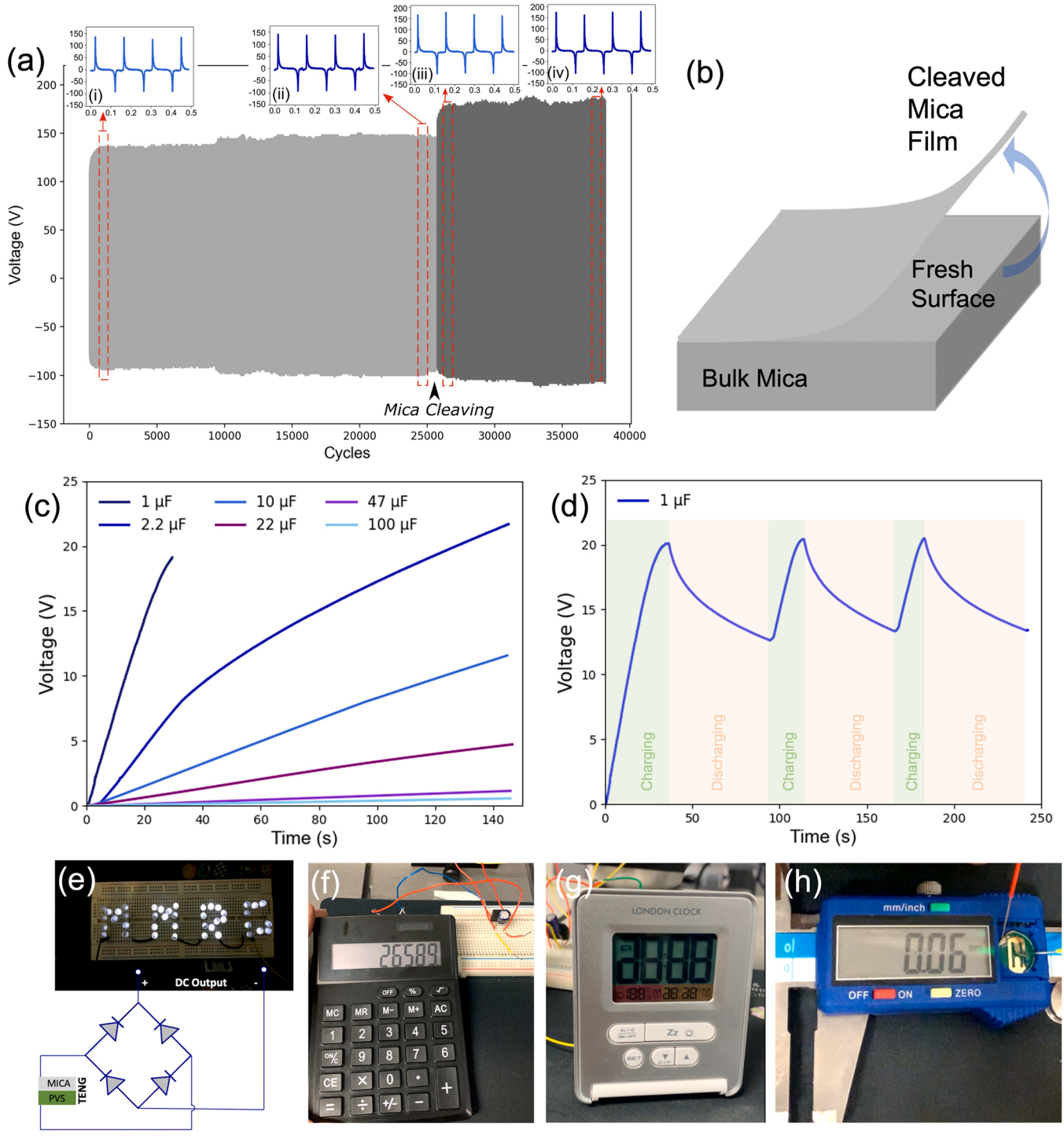

Fig. 13. (a) Long-term mechanical stability and durability test for Mica-FlatPVS TENG performed at a nominal contact pressure of 56 kPa and frequency of 7 Hz. Insets (i–iv) show zoomed-in views of electrical output signal and confirm the high uniformity and stability, (b) simplified schematic showing how a thin mica film is easily cleaved from the bulk sample to reveal a fresh layer, (c) charging characteristics of six different capacitors charged by the Mica-FlatPVS TENG and (d) charging-discharging characteristics of 1 μF capacitor. Real-time practical application demonstrations using the power generated by the Mica-FlatPVS TENG are shown next: (e) an array of 42 large-sized white LEDs forming the acronym 'MMRG', (f) a commercial calculator, (g) a digital alarm clock and (h) a digital micrometre display.

performance (peak power density of 4256 mW/m^2 for contact pressure of 64 kPa), but with the benefit of low-cost construction, good flexibility and ease of manufacture (i.e. no chemical modifications are required and the PVS can be rapidly moulded and cured). Fig. S8 in Supporting Information illustrates the flexibility of the device. A roughly indicative performance comparison with other TENG devices in the literature is given in Table S1 (Supplementary Information). Although direct comparison of TENG output from different works is challenging for various reasons (variations in frequency, surface roughness, pressure, layer thicknesses etc.), we can see that the max output power density is very much competitive with recently developed devices (second highest in Table S1). The approximate cost for developing a working model of the

Mica-PVS TENG comes out considerably lower than several other approaches giving comparable output (see Table S2 in Supporting Information for cost details).

4. Conclusions

TENGs are promising energy harvesters that generate electrical power from the rapid and repeated contact of a suitable tribo-electric material pair. However, the effect of the tribology and mechanics of the interface on TENG performance has not been explored comprehensively enough yet. This paper introduces a high-definition in-situ optical technique to image the real contact area developed at TENG interfaces. In addition, it develops a new type of TENG based on muscovite mica in contact with polyvinyl siloxane (or PVS). The new TENG and visualisation technique were then used to study how TENG electrical output responds to a wide variation in random multiscale surface roughness. Four instances of surface roughness were generated on the PVS surface (these were denoted according to their design roughness values as FlatPVS, PVS25, PVS50 and PVS100, but had measured roughness's of $Sq = 1.5$, 22.5, 40.5 and 82.5 μm). These were realised by 3D printing numerically designed multiscale rough surfaces and then moulding PVS tribo-layers from the 3D-printed master. The advantages of using a mica counter-surface include high dielectric strength, but crucially, high transparency to enable optical visualisation of the interface. Mica is also hard (compared to PVS) and near atomically smooth so that the contact scenario is equivalent to a rigid flat contacting a rough soft surface (the PVS).

The results show that electrical output is highly sensitive to surface roughness. The highest peak output power was found for the smoothest surface (FlatPVS with $Sq = 1.5$ μm) and this dropped by almost 70% when the roughness was increased as high as 82.5 μm (i.e. for PVS100). The in-situ interface imaging technique proved effective in accurately calculating the real contact area for each roughness. However, it is limited to the two-dimensional visualisation of contact area. Crucially, real contact area reduced similarly (to power) as surface roughness was increased, thus indicating that the roughness effect on contact area is the likely reason for the roughness sensitivity of TENG performance. Clearly solid-solid contact is more likely to promote triboelectric charge transfer across the interface. The smooth surface can facilitate a high contact area and this reduces as roughness increases due to deep valleys on the surface which are not likely to make contact at low and moderate pressures. As we mention, this result is not universal and can depend on relative material properties. For example, if a hard rough surface is pushed into a soft counter surface, TENG output might be expected to rise with increasing roughness. Likewise, materials with a high flexoelectric effect have been shown to be capable of increasing TENG output with increasing roughness. These results highlight the importance of understanding the contact area effect in TENG design because surface topography and material properties can clearly be chosen to optimise performance. The response of the Mica-PVS TENG to contact pressure and frequency was also explored: results confirm the characteristic increase in TENG output in response to increasing pressure or frequency, and in addition, show that TENG frequency and pressure response is more sensitive for smoother surfaces.

There were also some interesting findings on the testing of triboelectric nanogenerators: a very accurate mechanical testing approach (using an electrodynamic test machine) with surface self-alignment produced highly symmetric and uniform electrical output signals. The Mica-PVS TENG also showed excellent stability over large numbers of cycles and even exhibited a regenerative property where cleaving off a thin layer of mica after thousands of cycles produced a jump in output. The max output performance of the Mica-PVS TENG (achieved on the smoothest surface) was characterised by an open circuit voltage of 222.8 V, short circuit current density of 53 mA/m^2 and peak power density of 4256 mW/m^2. This represents competitive output performance, but with key advantages. These include rapid and simple fabrication procedure (PVS cures rapidly at room temperature), low cost, good flexibility, long durability and robustness. There are also no complex chemical modifications or fragile surface coatings required. Finally, the new Mica-PVS TENG, the in-situ optical interface characterisation approach and the findings on contact area and roughness are likely to be extremely useful in the future design of TENGs in several applications.

CRediT authorship contribution statement

Charchit Kumar: Conceptualization, Methodology, Software, Validation, Formal analysis, Visualization, Investigation, Writing – original draft, Writing – review & editing. **Jack Perris**: Methodology, Investigation. **Satyaranjan Bairagi**: Methodology, Investigation. **Guanbo Min**: Methodology, Investigation, **Yang Xu**: Conceptualization, Supervision, Writing – review & editing. **Nikolaj Gadegaard**: Supervision, Writing – review & editing, Funding acquisition. **Daniel M. Mulvihill**: Supervision, Conceptualization, Writing – original draft, Writing – review & editing, Project administration, Funding acquisition.

Declaration of Competing Interest

The authors declare that they have no known competing financial interests or personal relationships that could have appeared to influence the work reported in this paper.

Data availability

Data will be made available on request.

Acknowledgements

The authors acknowledge the support of the Leverhulme Trust under project grant "Fundamental Mechanical Behaviour of Nano and Micro Structured Interfaces" (RPG-2017-353). We also acknowledge the UK Engineering and Physical Sciences Research Council (EPSRC) for supporting the work through grant Ref. EP/V003380/1 ('Next Generation Energy Autonomous Textile Fabrics based on Triboelectric Nanogenerators'). We would also like to thank Dr Gaurav Khandelwal for his help with characterization. The authors also gratefully acknowledge support for the experimental work from the Taiho Kogyo Tribology Research Foundation (TTRF) in Japan under the 'Research Grant' entitled "Tribology of Triboelectric Nanogenerators: Understanding how Interface Mechanics effects Electrical Output" (which supported purchase of some of the key apparatus used). NG acknowledges funding from the Novo Nordisk Foundation Challenge Programme in Energy materials with biological applications (EMGUT): grant ref. No. NNF22OC0072961.

Appendix A. Supplementary information

Supplementary data associated with this article can be found in the online version at doi:10.1016/j.nanoen.2022.108122.

References

[1] A. Dewan, S.U. Ay, M.N. Karim, H. Beyenal, Alternative power sources for remote sensors: a review, J. Power Sources 245 (2014) 129–143, https://doi.org/10.1016/j.jpowsour.2013.06.081).
[2] Z.L. Wang, Triboelectric nanogenerator (TENG)—sparking an energy and sensor revolution, Adv. Energy Mater. 10 (2020) 2000137, https://doi.org/10.1002/aenm.202000137).
[3] W. Mrozik, M.A. Rajaeifar, O. Heidrich, P. Christensen, Environmental impacts, pollution sources and pathways of spent lithium-ion batteries, Energy Environ. Sci. 14 (2021) 6099–6121, https://doi.org/10.1039/D1EE00691F).
[4] R. Walden, C. Kumar, D.M. Mulvihill, S.C. Pillai, Opportunities and challenges in triboelectric nanogenerator (TENG) based sustainable energy generation technologies: a mini-review, Chem. Eng. J. Adv. 9 (2022), 100237, https://doi.org/10.1016/j.ceja.2021.100237).

[5] C. Wu, A.C. Wang, W. Ding, H. Guo, Z.L. Wang, Triboelectric nanogenerator: a foundation of the energy for the new era, Adv. Energy Mater. 9 (2019) 1802906, https://doi.org/10.1002/aenm.201802906).

[6] W.-G. Kim, D.-W. Kim, I.-W. Tcho, J.-K. Kim, M.-S. Kim, Y.-K. Choi, Triboelectric nanogenerator: structure, mechanism, and applications, ACS Nano 15 (2021) 258–287, https://doi.org/10.1021/acsnano.0c09803).

[7] Y. Wang, Y. Yang, Z.L. Wang, Triboelectric nanogenerators as flexible power sources, npj Flex. Electron. 1 (2017) 1–10, https://doi.org/10.1038/s41528-017-0007-8).

[8] S. Niu, Y. Liu, S. Wang, L. Lin, Y.S. Zhou, Y. Hu, Z.L. Wang, Theory of sliding-mode triboelectric nanogenerators, Adv. Mater. 25 (2013) 6184–6193, https://doi.org/10.1002/adma.201302808).

[9] D.W. Kim, J.H. Lee, J.K. Kim, U. Jeong, Material aspects of triboelectric energy generation and sensors, NPG Asia Mater. 12 (2020) 1–17, https://doi.org/10.1038/s41427-019-0176-0).

[10] R. Zhang, H. Olin, Material choices for triboelectric nanogenerators: a critical review, EcoMat 2 (2020), e12062, https://doi.org/10.1002/eom2.12062).

[11] J. Henniker, Triboelectricity in polymers, 474–474, Nature 196 (1962), https://doi.org/10.1038/196474a0).

[12] H. Zou, et al., Quantifying the triboelectric series, Nat. Commun. 10 (2019) 1427, https://doi.org/10.1038/s41467-019-09461-x).

[13] A. Chen, C. Zhang, G. Zhu, Z.L. Wang, Polymer materials for high-performance triboelectric nanogenerators, Adv. Sci. 7 (2020) 2000186, https://doi.org/10.1002/advs.202000186).

[14] A.L. Andrady, M.A. Neal, Applications and societal benefits of plastics, Philos. Trans. R Soc. Lond. B Biol. Sci. 364 (2009) 1977–1984, https://doi.org/10.1098/rstb.2008.0304).

[15] G. Min, Y. Xu, P. Cochran, N. Gadegaard, D.M. Mulvihill, R. Dahiya, Origin of the contact force-dependent response of triboelectric nanogenerators, Nano Energy 83 (2021), 105829, https://doi.org/10.1016/j.nanoen.2021.105829).

[16] H. Zhang, Y. Lu, A. Ghaffarinejad, P. Basset, Progressive contact-separate triboelectric nanogenerator based on conductive polyurethane foam regulated with a Bennet doubler conditioning circuit, Nano Energy 51 (2018) 10–18, https://doi.org/10.1016/j.nanoen.2018.06.038).

[17] S. Wang, L. Lin, Y. Xie, Q. Jing, S. Niu, Z.L. Wang, Sliding-triboelectric nanogenerators based on in-plane charge-separation mechanism, Nano Lett. 13 (2013) 2226–2233, https://doi.org/10.1021/nl400738p).

[18] P. Zhang, W. Zhang, H. Zhang, A triboelectric nanogenerator based on waste polyvinyl chloride for Morse code generator, Sens. Actuators A Phys. 322 (2021), 112633, https://doi.org/10.1016/j.sna.2021.112633).

[19] F.R. Fan, J. Luo, W. Tang, C. Li, C. Zhang, Z. Tian, Z.L. Wang, Highly transparent and flexible triboelectric nanogenerators: performance improvements and fundamental mechanisms, J. Mater. Chem. A 2 (2014) 13219–13225, https://doi.org/10.1039/C4TA02747G).

[20] Y. Xu, G. Min, N. Gadegaard, R. Dahiya, D.M. Mulvihill, A unified contact force-dependent model for triboelectric nanogenerators accounting for surface roughness, Nano Energy 76 (2020), 105067, https://doi.org/10.1016/j.nanoen.2020.105067).

[21] C.-C. Wang, C.-Y. Chang, Enhanced output performance and stability of triboelectric nanogenerators by employing silane-based self-assembled monolayers, J. Mater. Chem. C 8 (2020) 4542–4548, https://doi.org/10.1039/D0TC00041H).

[22] G.-Z. Li, et al., A high-performance transparent and flexible triboelectric nanogenerator based on hydrophobic composite films, Nano Energy 75 (2020), 104918, https://doi.org/10.1016/j.nanoen.2020.104918).

[23] D. Jing, Y. Pan, D. Li, X. Zhao, B. Bhushan, Effect of surface charge on the nanofriction and its velocity dependence in an electrolyte based on lateral force microscopy, Langmuir 33 (2017) 1792–1798, https://doi.org/10.1021/acs.langmuir.6b04332).

[24] C. Wu, T.W. Kim, J.H. Park, H. An, J. Shao, X. Chen, Z.L. Wang, Enhanced triboelectric nanogenerators based on MoS2 monolayer nanocomposites acting as electron-acceptor layers, ACS Nano 11 (2017) 8356–8363, https://doi.org/10.1021/acsnano.7b03657).

[25] G. Song, et al., Molecularly engineered surface triboelectric nanogenerator by self-assembled monolayers (METS), Chem. Mater. 27 (2015) 4749–4755, https://doi.org/10.1021/acs.chemmater.5b01507).

[26] Y. Yu, X. Wang, Chemical modification of polymer surfaces for advanced triboelectric nanogenerator development, Extrem. Mech. Lett. 9 (2016) 514–530, https://doi.org/10.1016/j.eml.2016.02.019).

[27] Y. Zheng, L. Cheng, M. Yuan, Z. Wang, L. Zhang, Y. Qin, T. Jing, An electrospun nanowire-based triboelectric nanogenerator and its application in a fully self-powered UV detector, Nanoscale 6 (2014) 7842–7846, https://doi.org/10.1039/C4NR01934B).

[28] Y. Kim, X. Wu, J.H. Oh, Fabrication of triboelectric nanogenerators based on electrospun polyimide nanofibers membrane, Sci. Rep. 10 (2020) 2742, https://doi.org/10.1038/s41598-020-59546-7).

[29] S.M.S. Rana, M.T. Rahman, M. Salauddin, S. Sharma, P. Maharjan, T. Bhatta, H. Cho, C. Park, J.Y. Park, Electrospun PVDF-TrFE/MXene nanofiber mat-based triboelectric nanogenerator for smart home appliances, ACS Appl. Mater. Interfaces 13 (2021) 4955–4967, https://doi.org/10.1021/acsami.0c17512).

[30] G. Min, A. Pullanchiyodan, A.S. Dahiya, E.S. Hosseini, Y. Xu, D.M. Mulvihill, R. Dahiya, Ferroelectric-assisted high-performance triboelectric nanogenerators based on electrospun P(VDF-TrFE) composite nanofibers with barium titanate nanofillers, Nano Energy 90 (2021), 106600, https://doi.org/10.1016/j.nanoen.2021.106600).

[31] S.M. Harstad, P. Zhao, N. Soin, A.A. El-Gendy, S. Gupta, V.K. Pecharsky, J. Luo, R. L. Hadimani, Gd_5Si_4 -PVDF nanocomposite films and their potential for triboelectric energy harvesting applications, AIP Adv. 9 (2019), 035116, https://doi.org/10.1063/1.5080116).

[32] Z. Li, X. Wang, Y. Hu, L. Li, C. Wang, Triboelectric properties of BaTiO3/polyimide nanocomposite film, Appl. Surf. Sci. 572 (2022), 151391, https://doi.org/10.1016/j.apsusc.2021.151391).

[33] S. Ippili, V. Jella, A.M. Thomas, C. Yoon, J.-S. Jung, S.-G. Yoon, ZnAl–LDH-induced electroactive β-phase and controlled dielectrics of PVDF for a high-performance triboelectric nanogenerator for humidity and pressure sensing applications, J. Mater. Chem. A 9 (2021) 15993–16005, https://doi.org/10.1039/D1TA02966E).

[34] H.-J. Choi, J.H. Lee, J. Jun, T.Y. Kim, S.-W. Kim, H. Lee, High-performance triboelectric nanogenerators with artificially well-tailored interlocked interfaces, Nano Energy 27 (2016) 595–601, https://doi.org/10.1016/j.nanoen.2016.08.014).

[35] F.-R. Fan, L. Lin, G. Zhu, W. Wu, R. Zhang, Z.L. Wang, Transparent triboelectric nanogenerators and self-powered pressure sensors based on micropatterned plastic films, Nano Lett. 12 (2012) 3109–3114, https://doi.org/10.1021/nl300988z).

[36] W. Yang, X. Wang, H. Li, J. Wu, Y. Hu, Z. Li, H. Liu, Fundamental research on the effective contact area of micro-/nano-textured surface in triboelectric nanogenerator, Nano Energy 57 (2019) 41–47, https://doi.org/10.1016/j.nanoen.2018.12.029).

[37] D. Kim, et al., Direct-laser-patterned friction layer for the output enhancement of a triboelectric nanogenerator, Nano Energy 35 (2017) 379–386, https://doi.org/10.1016/j.nanoen.2017.04.013).

[38] M.-L. Seol, S.-H. Lee, J.-W. Han, D. Kim, G.-H. Cho, Y.-K. Choi, Impact of contact pressure on output voltage of triboelectric nanogenerator based on deformation of interfacial structures, Nano Energy 17 (2015) 63–71, https://doi.org/10.1016/j.nanoen.2015.08.005).

[39] C. Jin, D.S. Kia, M. Jones, S. Towfighian, On the contact behavior of micro-/nano-structured interface used in vertical-contact-mode triboelectric nanogenerators, Nano Energy 27 (2016) 68–77, https://doi.org/10.1016/j.nanoen.2016.06.049).

[40] J. Huang, X. Fu, G. Liu, S. Xu, X. Li, C. Zhang, L. Jiang, Micro/nano-structures-enhanced triboelectric nanogenerators by femtosecond laser direct writing, Nano Energy 62 (2019) 638–644, https://doi.org/10.1016/j.nanoen.2019.05.081).

[41] B.A. Krick, J.R. Vail, B.N. Persson, W.G. Sawyer, Optical in situ micro tribometer for analysis of real contact area for contact mechanics, adhesion, and sliding experiments, Tribol. Lett. 45 (2012) 185–194, https://doi.org/10.1007/s11249-011-9870-y).

[42] C. Kumar, D. Favier, T. Speck, V.L. Houérou, In situ investigation of adhesion mechanisms on complex microstructured biological surfaces, Adv. Mater. Interfaces 7 (2020) 2000969, https://doi.org/10.1002/admi.202000969).

[43] L.E. Helseth, Optical force sensing principle based on transparent elastomer with a rough surface, Sens. Actuators A Phys. 263 (2017) 667–676, https://doi.org/10.1016/j.sna.2017.07.033).

[44] J.S. Sharp, S.F. Poole, B.W. Kleiman, Optical measurement of contact forces using frustrated total internal reflection, Phys. Rev. Appl. 10 (2018), 034051, https://doi.org/10.1103/PhysRevApplied.10.034051).

[45] C. Kumar, T. Speck, Le, V. Houérou, Local contact formation during sliding on soft adhesive surfaces with complex microstructuring, Tribol. Int. 163 (2021), 107180, https://doi.org/10.1016/j.triboint.2021.107180).

[46] M.H. Müser, et al., Meeting the contact-mechanics challenge, Tribol. Lett. 65 (2017) 118, https://doi.org/10.1007/s11249-017-0900-2).

[47] M.N. Mandikos, Polyvinyl siloxane impression materials: an update on clinical use, Aust. Dent. J. 43 (1998) 428–434, https://doi.org/10.1111/j.1834-7819.1998.tb00204.x).

[48] G. Mazzanti, C. Daniele, B. Tita, F. Vitali, A. Signore, Biological evaluation of a polyvinyl siloxane impression material, Dent. Mater. 21 (2005) 371–374, https://doi.org/10.1016/j.dental.2004.06.004).

[49] J. Perris, C. Kumar, Y. Xu, M. Tassieri, M.E. Kartal, N. Gadegaard, D.M. Mulvihill, 3D printing and rapid replication of advanced numerically generated rough surface topographies in numerous polymers, Adv. Eng. Mater. (2022).

[50] M. Nasiri, S.M. Rozati, Muscovite mica as a flexible substrate for transparent conductive AZO thin films deposited by spray pyrolysis, Mater. Sci. Semicond. Process. 81 (2018) 38–43, https://doi.org/10.1016/j.mssp.2018.03.009).

[51] J.C. Contreras-Naranjo, J.A. Silas, V.M. Ugaz, Reflection interference contrast microscopy of arbitrary convex surfaces, Appl. Opt. 49 (2010) 3701–3712, https://doi.org/10.1364/AO.49.003701).

[52] H.K. Christenson, N.H. Thomson, The nature of the air-cleaved mica surface, Surf. Sci. Rep. 71 (2016) 367–390, https://doi.org/10.1016/j.surfrep.2016.03.001).

[53] D.W. Jin, Y.J. Ko, D.S. Kong, H.K. Kim, J.-H. Ha, M. Lee, J.-I. Hong, J.H. Jung, Thermal stability and Young's modulus of mechanically exfoliated flexible mica, Curr. Appl. Phys. 18 (2018) 1486–1491, https://doi.org/10.1016/j.cap.2018.09.002).

[54] D.W. Dye, L. Hartshorn, The dielectric properties of mica, Proc. Phys. Soc. Lond. 37 (1924) 42–57, https://doi.org/10.1088/1478-7814/37/1/304).

[55] J. Perris, Y. Xu, M.E. Kartal, N. Gadegaard, D.M. Mulvihill, Tailorable and repeatable normal contact stiffness via micropatterned interfaces, Tribol. Lett. 69 (2021) 106, https://doi.org/10.1007/s11249-021-01473-3).

[56] D. Hong, Y.-M. Choi, J. Jeong, Test bed for contact-mode triboelectric nanogenerator, Rev. Sci. Instrum. 89 (2018), 065110, https://doi.org/10.1063/1.5027764).

[57] S.S.K. Mallineni, H. Behlow, R. Podila, A.M. Rao, A low-cost approach for measuring electrical load currents in triboelectric nanogenerators, Nanotechnol. Rev. 7 (2018) 149–156, https://doi.org/10.1515/ntrev-2017-0178).

[58] I. Weber, [2] Reflection interference contrast microscopy. Methods in Enzymology, Academic Press, 2003, pp. 34–47, https://doi.org/10.1016/S0076-6879(03)61004-9).
[59] M.M. Chaudhri, E.H. Yoffe, The area of contact between a small sphere and a flat surface, Philos. Mag. A 44 (1981) 667–675, https://doi.org/10.1080/01418618108236169).
[60] J. Schindelin, et al., Fiji: an open-source platform for biological-image analysis, Nat. Methods 9 (2012) 676–682, https://doi.org/10.1038/nmeth.2019).
[61] C. Kumar, V. Le Houérou, T. Speck, H.F. Bohn, Straightforward and precise approach to replicate complex hierarchical structures from plant surfaces onto soft matter polymer, R. Soc. Open Sci. 5 (2018), 172132, https://doi.org/10.1098/rsos.172132).
[62] R.D.I.G. Dharmasena, Inherent asymmetry of the current output in a triboelectric nanogenerator, Nano Energy 76 (2020), 105045, https://doi.org/10.1016/j.nanoen.2020.105045).
[63] A. Ibrahim, M. Jain, E. Salman, R. Willing, S. Towfighian, A smart knee implant using triboelectric energy harvesters, Smart Mater. Struct. 28 (2019), 025040, https://doi.org/10.1088/1361-665X/aaf3f1).
[64] J. Wen, H. He, C. Niu, M. Rong, Y. Huang, Y. Wu, An improved equivalent capacitance model of the triboelectric nanogenerator incorporating its surface roughness, Nano Energy 96 (2022), 107070, https://doi.org/10.1016/j.nanoen.2022.107070).
[65] B.N.J. Persson, Contact mechanics for randomly rough surfaces, Surf. Sci. Rep. 61 (2006) 201–227, https://doi.org/10.1016/j.surfrep.2006.04.001).
[66] V. Hisler, M. Palmieri, V. Le Houérou, C. Gauthier, M. Nardin, M.-F. Vallat, L. Vonna, Scale invariance of the contact mechanics of micropatterned elastic substrates, Int. J. Adhes. Adhes. 45 (2013) 144–149, https://doi.org/10.1016/j.ijadhadh.2013.04.006).
[67] V.A. Yastrebov, G. Anciaux, J.-F. Molinari, From infinitesimal to full contact between rough surfaces: evolution of the contact area, Int. J. Solids Struct. 52 (2015) 83–102, https://doi.org/10.1016/j.ijsolstr.2014.09.019).
[68] J. Sintusiri, V. Harnchana, V. Amornkitbamrung, A. Wongsa, P. Chindaprasirt, Portland cement-TiO2 triboelectric nanogenerator for robust large-scale mechanical energy harvesting and instantaneous motion sensor applications, Nano Energy 74 (2020), 104802, https://doi.org/10.1016/j.nanoen.2020.104802).
[69] R.D.I.G. Dharmasena, K.D.G.I. Jayawardena, C.A. Mills, J.H.B. Deane, J.V. Anguita, R.A. Dorey, S.R.P. Silva, Triboelectric nanogenerators: providing a fundamental framework, Energy Environ. Sci. 10 (2017) 1801–1811, https://doi.org/10.1039/C7EE01139C.
[70] T. Huang, M. Lu, H. Yu, Q. Zhang, H. Wang, M. Zhu, Enhanced power output of a triboelectric nanogenerator composed of electrospun nanofiber mats doped with graphene oxide, Sci. Rep. 5 (2015) 13942, https://doi.org/10.1038/srep13942).
[71] Z. Saadatnia, S.G. Mosanenzadeh, E. Esmailzadeh, H.E. Naguib, A high performance triboelectric nanogenerator using porous polyimide aerogel film, Sci. Rep. 9 (2019) 1370, https://doi.org/10.1038/s41598-018-38121-1).
[72] R.D.I.G. Dharmasena, J.H.B. Deane, S.R.P. Silva, Nature of power generation and output optimization criteria for triboelectric nanogenerators, Adv. Energy Mater. 8 (2018) 1802190, https://doi.org/10.1002/aenm.201802190).
[73] H. Wang, L. Xu, Y. Bai, Z.L. Wang, Pumping up the charge density of a triboelectric nanogenerator by charge-shuttling, Nat. Commun. 11 (2020) 4203, https://doi.org/10.1038/s41467-020-17891-1).
[74] L. Lin, S. Wang, S. Niu, C. Liu, Y. Xie, Z.L. Wang, Noncontact free-rotating disk triboelectric nanogenerator as a sustainable energy harvester and self-powered mechanical sensor, ACS Appl. Mater. Interfaces 6 (2014) 3031–3038, https://doi.org/10.1021/am405637s).
[75] J.H. Lee, I. Yu, S. Hyun, J.K. Kim, U. Jeong, Remarkable increase in triboelectrification by enhancing the conformable contact and adhesion energy with a film-covered pillar structure, Nano Energy 34 (2017) 233–241, https://doi.org/10.1016/j.nanoen.2017.02.032).
[76] C. Heinert, R.M. Sankaran, D.J. Lacks, Decay of electrostatic charge on surfaces due solely to gas phase interactions, J. Electrost. 115 (2022), 103663, https://doi.org/10.1016/j.elstat.2021.103663).
[77] B.X. Du, Z.L. Li, J. Li, Surface charge accumulation and decay of direct-fluorinated RTV silicone rubber, IEEE Trans. Dielectr. Electr. Insul. 21 (2014) 2338–2342, https://doi.org/10.1109/TDEI.2014.004079).
[78] A. Crisci, B. Gosse, J.-P. Gosse, V. Ollier-Duréault, Surface-potential decay due to surface conduction, Eur. Phys. J. AP 4 (1998) 107–116, https://doi.org/10.1051/epjap:1998249).
[79] J.A. Greenwood, J.H. Tripp, The elastic contact of rough spheres, J. Appl. Mech. 34 (1967) 153–159, https://doi.org/10.1115/1.3607616).
[80] M. Scaraggi, B.N.J. Persson, General contact mechanics theory for randomly rough surfaces with application to rubber friction, J. Chem. Phys. 143 (2015), 224111, https://doi.org/10.1063/1.4936558).
[81] S. Dalvi, A. Gujrati, S.R. Khanal, L. Pastewka, A. Dhinojwala, T.D.B. Jacobs, Linking energy loss in soft adhesion to surface roughness, PNAS 116 (2019) 25484–25490, https://doi.org/10.1073/pnas.1913126116).
[82] R. Ledesma-Alonso, E. Raphael, F. Restagno, C. Poulard, Effect of the density of pillar-patterned substrates on contact mechanics: transition from top to mixed contact with a detailed pressure-field description, Phys. Rev. E 104 (2021), 055007, https://doi.org/10.1103/PhysRevE.104.055007).
[83] B. Persson, E. Tosatti, The effect of surface roughness on the adhesion of elastic solids, J. Chem. Phys. 115 (2001) 5597–5610, https://doi.org/10.1063/1.1398300).
[84] T.T. Duncan, E.P. Chan, K.L. Beers, Maximizing contact of supersoft bottlebrush networks with rough surfaces to promote particulate removal, ACS Appl. Mater. Interfaces 11 (2019) 45310–45318, https://doi.org/10.1021/acsami.9b17602).
[85] H. Qiao, et al., Mixed triboelectric and flexoelectric charge transfer at the nanoscale, Adv. Sci. 8 (2021) 2101793, https://doi.org/10.1002/advs.202101793).
[86] Z. Li, Z. Zhou, Y. Li, S. Tang, Effect of cyclic loading on surface instability of silicone rubber under compression, Polymers 9 (2017) 148, https://doi.org/10.3390/polym9040148).
[87] T. Gejguš, J. Schröder, K. Loos, A. Lion, M. Johlitz, Advanced characterisation of soft polymers under cyclic loading in context of engine mounts, Polymers 14 (2022) 429, https://doi.org/10.3390/polym14030429).
[88] H.K. Christenson, Adhesion and surface energy of mica in air and water, J. Phys. Chem. 97 (1993) 12034–12041, https://doi.org/10.1021/j100148a032).

Charchit Kumar is a Research Associate in the Materials & Manufacturing Research Group (MMRG) within the School of Engineering at the University of Glasgow, UK. He obtained his joint-PhD in the field of tribology at Freiburg Centre for Interactive Materials & Bioinspired Technologies, University of Freiburg (Germany) and Institut Charles Sadron (CNRS), University of Strasbourg (France). His PhD research was focused on adhesion and friction mechanics on complex microstructured surfaces. Following his PhD, he was Postdoctoral Research & Teaching Associate at the Laboratoire ICube (CNRS), University of Strasbourg. Currently, his research focuses on contact mechanics, triboelectric nanogenerators, flexoelectricity, materials engineering, and electro-adhesion.

Jack Perris is a Postdoctoral Researcher in Mechanical Engineering at the University of Glasgow, James Watt School of Engineering. He recently completed his PhD in Mechanical Engineering at the University of Glasgow within the Materials and Manufacturing Research Group (MMRG). He currently works at the Centre for Medical and Industrial Ultrasonics (University of Glasgow) focussing on gas pipeline monitoring. His research interests focus on materials engineering, surface fabrication, tribology, and advanced manufacturing.

Satyaranjan Bairagi is a postdoctoral fellow within the School of Engineering at the University of Glasgow UK. He completed his Ph.D. in Materials Science from Indian Institute of Technology- Delhi, India. His research interests include development of nanotechnology based piezoelectric and triboelectric materials for nanogenerators as well as textile based flexible advanced materials for renewable energy harvesting. He has published numerous research articles in various reputed peer-reviewed journals. In addition, Dr. Bairagi has published and written more than 30 book chapters which have been published and submitted in different books under various publishers such as Elsevier, Wiley, Springer and so forth.

Guanbo Min received a B.Sc. degree in Electronic Information Technology from Macau University of Science and Technology, Macao S.A.R, China in 2015 and a M.Sc. degree in Electronics and Electrical Engineering from University of Glasgow in 2017. He gained his Ph.D. degree from the University of Glasgow in 2022 for work on optimising various aspects of the normal contact mode triboelectric nanogenerator. Also in 2022, Dr Min was appointed as an Assistant Professor at Ningbo University in China.

Yang Xu is a Research Professor in mechanical engineering at Hefei University of Technology (China). He received his M.S and Ph.D. degrees in mechanical engineering at Auburn University (USA) in 2012 and 2017, respectively. From 2018 to 2020, he was a Research Associate at University of Glasgow (UK). He has research interests in the fundamentals of contact mechanics and its applications in multidisciplinary fields, e.g., tribology, contact-/tribo-electrification, triboelectric nanogenerator, etc.

Nikolaj Gadegaard FRSE is Professor of Biomedical Engineering and Director of Research in the School of Engineering at the University of Glasgow. He has an educational background in Chemistry, Physics and Biophysics, and has worked at the interface of physics/engineering and biology for more than two decades. He is an expert on the use of micro- and nanofabrication technologies for biomedical applications with a particular focus on using injection moulding. He has published 200 papers in e.g. Nature family journals, Advanced Materials and ACS with $>$ 18.000 citations and an h-index of 57. In 2015 he received an ERC consolidator grant.

Daniel M. Mulvihill is Senior Lecturer (Associate Professor) in Mechanical Engineering at the University of Glasgow James Watt School of Engineering. He completed a D.Phil. in Engineering Science at the University of Oxford in 2012 and subsequently undertook postdoctoral periods at the University of Limerick, EPFL Switzerland and the University of Cambridge prior to joining Glasgow in 2016. His interests are mainly focused on materials engineering, tribology and materials for energy applications. Dr Mulvihill is a former Institution of Mechanical Engineers (IMechE) Tribology Trust Bronze Medallist (2013). He presently leads a major £1.5 M EPSRC project (EP/V003380/1) on next generation textile triboelectric nanogenerators. Dr Mulvihill is a 'Novel Materials' Editor for *Chemical Engineering Journal* (Elsevier) and an Associate Editor for *Results in Engineering* (Elsevier).